Design, Dynamic Modeling, and Motion Analysis of a Frog-Inspired Hybrid-Driven Amphibious Robot

Yitao Pan , Libing Hu , Yongsheng Ou * , Jizhuang Fan

Posted Date: 2 May 2026

doi: 10.20944/preprints202604.2226.v1

Keywords: frog-inspired amphibious robot; jumping locomotion; swimming locomotion; hybrid drive

 doi:10.20944/preprints202604.2226.v1

Article

Design, Dynamic Modeling, and Motion Analysis of a Frog-Inspired Hybrid-Driven Amphibious Robot

Yitao Pan [1], Libing Hu [1], Yongsheng Ou [1,*] and Jizhuang Fan [2]

[1] School of Control Science and Engineering, Dalian University of Technology, Linggong Road 2, Dalian, Liaoning Province 116024, China

[2] State Key Laboratory of Robotics and System, Harbin Institute of Technology (HIT), Harbin, China

* Correspondence: yoo2023@dlut.edu.cn

Highlights

The robot innovatively combines an explosion-driven hind limb activation mechanism with a rope-driven swimming system, enabling it to achieve frog-like jumping and swimming capabilities on both land and water, thus avoiding complex structural transitions when switching between environments.Additionally, By establishing an amphibious dynamic model and constructing an experimental prototype, the study validated the robot's amphibious mobility and the correctness and effectiveness of its dynamic theory, ensuring high-performance operation in different environments.

Abstract

In order to enhance the amphibious mobility of robots in water-land environments, this paper proposes a frog-inspired hybrid drive amphibious robot, based on the amphibious locomotion characteristics of frogs. Distinct from existing single-mode frog-inspired jumping or swimming robots, the proposed robot innovatively integrates hybrid propulsion to simultaneously achieve both frog-like swimming and jumping capabilities. On land, the robot utilizes an explosion-driven hind limb actuation mechanism, paired with a linkage-based forelimb posture control system, to achieve high-performance frog-like jumping. In water, a rope-driven hind limb mechanism facilitates extension and retraction movements, while controllable soft-actuated flippers enable swinging and opening/closing motions, thereby achieving efficient frog-like swimming. In addition, an amphibious dynamic model was developed, and the robot's amphibious locomotion capabilities were evaluated and analyzed. Finally, an experimental prototype platform was built to test the amphibious locomotion performance of the designed robot, and a comparative analysis was conducted with the theoretical model. The experimental results not only validated the correctness of the amphibious dynamics and motion theory, but also confirmed the effectiveness of the designed amphibious terrain-crossing mechanism.

Keywords: frog-inspired amphibious robot; jumping locomotion; swimming locomotion; hybrid drive

1. Introduction

In recent years, with the rapid development of science and technology, significant research breakthroughs have been made in various fields, including sensors, novel materials [1–4], 3D printing [5,6], and artificial intelligence. This advancement has effectively accelerated the rapid development of robotics technology, enhancing its integrated operational capabilities, enabling robots to take on more high-risk or difficult tasks that are challenging for humans to accomplish. However, the application scenarios of robots have gradually expanded from the initial unit-based manufacturing environments to various complex domains, including domestic services, battlefield operations, and high-radiation extreme environments in the nuclear industry [7,8].Therefore, certain special tasks,

 doi:10.20944/preprints202604.2226.v1

such as geological disaster rescue, riverbed shallow exploration, and amphibious battlefield reconnaissance, require robots to ensure the successful completion of tasks in various environments. With changes in environmental conditions, the locomotion modes of robots must also adapt accordingly. Generally, robots with a single locomotion mode are limited to operation in specific environments. For example, aerial robots [9] are capable of flying in the air but lack ground locomotion mechanisms, making them unsuitable for terrestrial movement. Ground mobile robots [10] exhibit effective mobility on land but are unable to operate underwater due to the absence of underwater propulsion systems. Similarly, underwater robots [11] can maneuver freely in aquatic environments, but the lack of aerial and terrestrial mobility mechanisms prevents them from adapting to land and air environments.In contrast to the aforementioned single-mode mobile robots, multi-modal mobile robots are designed with specialized structures that enable them to perform tasks across multiple environments. As a result, this type of robot [12–17] has garnered increasing attention and interest from researchers. Among them, amphibious mobile robots have shown great potential for application in both aquatic and terrestrial environments [18,19]. They are widely used in fields such as scientific exploration, marine ecological monitoring, and underwater resource exploration, and also play a crucial role in tasks like natural disaster rescue, military reconnaissance, and coastal patrols [20–24]. Therefore, addressing the structural design, kinematic modeling, and motion planning of amphibious robots to meet the demands of both aquatic and terrestrial operations is of significant practical importance [25,26].

However, existing amphibious robots mostly rely on traditional locomotion systems such as wheeled, tracked, legged, or hybrid mechanisms to perform cross-medium operations. As shown in figure 1(a), in 2024, Lu [27] from Huazhong University of Science and Technology, proposed a wheel-propeller-based amphibious robot with variable-pitch propellers. By adjusting the pitch angle of the propeller blades, the robot is capable of fast and stable locomotion on flat terrain, obstacle traversal, and omnidirectional movement on water surfaces. In 2025, Sato [28] from Okayama University of Science, proposed a multi-joint propeller-based amphibious robot, as shown in figure 1(b). By altering the joint orientation of the leg mechanism with a planar hinge, the robot achieves stable locomotion on both land and water surfaces. In 2023, Xu [29] from Hohai University, proposed a screw propulsion-based amphibious robot, as shown in figure 1(c). By optimizing and designing the height and pitch of the screw blades, the robot achieves improved adaptability in semi-fluid amphibious environments, such as marshes and mudflats. In 2025, Hu [30] from Anhui Jianzhu University, proposed a hybrid wheel-paddle-leg integrated amphibious robot, as shown in figure 1(d). By utilizing a composite wheel based on a planetary gear mechanism, the circular wheel can morph into a paddle-leg configuration, enabling the robot to achieve multiple locomotion modes. This design allows the amphibious robot to operate effectively across diverse task environments. In summary, wheeled mechanisms feature simple structures, high propulsion efficiency, and ease of control, but exhibit limited environmental adaptability. Tracked and legged mechanisms offer strong obstacle-surmounting capabilities, yet are heavier, structurally more complex, and less maneuverable. Hybrid locomotion systems demonstrate better adaptability to complex environments; however, their mechanical structures and control systems are relatively complex to design. Overall, conventional amphibious robots are mature, reliable, and efficient, but are significantly constrained by terrain conditions, making them less effective in unfamiliar or complex operational environments.

 doi:10.20944/preprints202604.2226.v1

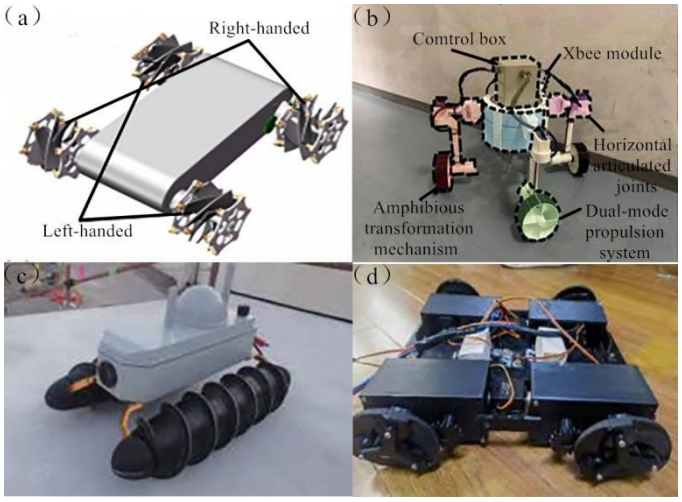

Figure 1. Traditional drive-type amphibious robots: (a) Variable wheel-propeller type [27]; (b) Multi-joint propeller type [28]; (c) Screw propulsion type [29]; (d) Wheel-propeller-leg integrated hybrid type [30].

Compared to traditional drive-type amphibious robots, biomimetic amphibious robots are inspired by the high flexibility [31] and strong adaptability [32,33] exhibited by biological organisms in unstructured and dynamic environments, which enables the robot to have a richer and more flexible movement mode. This provides more design ideas for executing amphibious tasks in complex environments [34]. As shown in figure 2(a), in 2022, Yale University in the United States [35], inspired by the locomotion characteristics of ancient sea turtles, developed a biomimetic amphibious robot. The robot utilizes variable stiffness materials to construct limbs with flippers. On land, the stiffness of the limb flippers is increased to make them rigid, enabling the robot to walk with a turtle-like limb oscillation. Once in the water, the stiffness of the flippers is reduced, transforming the limbs into fin-like appendages, allowing the robot to glide and swim in a turtle-like manner. In 2022, the University of Illinois in the United States [36], inspired by the locomotion mechanism of seals, developed a biomimetic amphibious robot, as shown in figure 2(b). The robot consists of a wave-like deformable backbone mechanism and a spindle-shaped deformable support structure. By designing actuators based on shape memory alloys, the robot achieves rapid swimming in water and crawling motion on land. Similarly, in 2023, a research team from the National University of Defense Technology in China [37], inspired by the undulating fin propulsion of aquatic animals, developed a biomimetic finned amphibious robot, as shown in figure 2(c). A series of undulating fin mechanisms were designed on both sides of the robot. Driven by composite wave motions, the robot is capable of fin-like swimming in water and crawling on land. In 2024, a research team from Nankai University [38], inspired by the undulatory motion of the flexible fins of stingrays, designed a novel traveling-wave driven biomimetic stingray amphibious robot, as shown in figure 2(d). The team developed a traveling-wave drive mechanism that converts the rotational motion of a motor into sinusoidal waves through a spiral rod passing through a series of aligned movable hinges. This design enhances both the robot's mobility and its obstacle-crossing capability.

 doi:10.20944/preprints202604.2226.v1

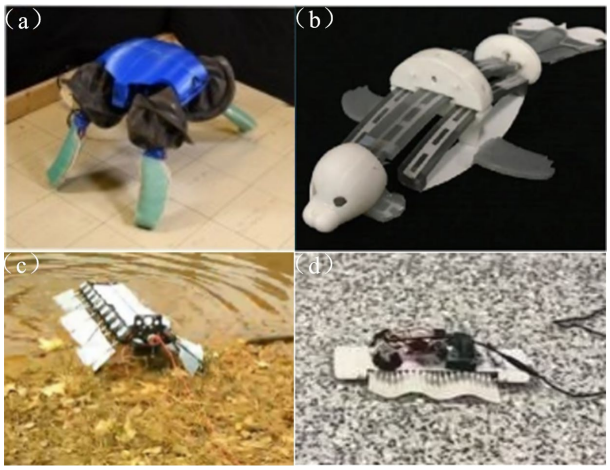

Figure 2. Biomimetic amphibious robots: (a) Biomimetic sea turtle amphibious robot [35]; (b) Biomimetic sea lion amphibious robot [36]; (c) Biomimetic fin amphibious robot [37]; (d) Biomimetic stingray amphibious robot [38].

Despite the breakthroughs in mimicking the motion characteristics of natural organisms, the aforementioned bionic amphibious robot design still presents some drawbacks. For example, the robot continues to rely on complex deformation structures and driving mechanisms, which results in a more intricate control system and higher susceptibility to malfunctions. Additionally, significant energy loss occurs during the deformation process, particularly when transitioning between aquatic and terrestrial environments, potentially leading to a decrease in efficiency. Therefore, the ability to adapt to both aquatic and terrestrial environments poses significant challenges [39,40] to the design and development of biomimetic amphibious robots, particularly in terms of their body structure, propulsion mechanisms, and motion control. Compared to organisms such as turtles, seals, and rays, frogs, as typical amphibians, have a compact body and light weight, along with excellent swimming and jumping abilities both in water and on land. Inspired by the amphibious locomotion mechanism of frogs, a biomimetic amphibious robot was developed, capable of high-explosive jumps and swimming, while also exhibiting exceptional amphibious agility. As shown in figure 3(a), in 2007, Ryuma Niiyama and his team from the University of Tokyo [41], inspired by the skeletal features of frogs, developed a bipedal, multi-joint biomimetic frog jumping robot. The robot's pneumatic muscles contract to drive the extension of its multi-jointed hind limbs, enabling it to achieve a vertical jump of up to 260mm. In 2013, the Korea Advanced Institute of Science and Technology (KAIST) [42] developed a frog-inspired jumping robot, as shown in figure 3(b), based on the structural principles of frog skeletal muscles. The robot utilizes a four-bar linkage mechanism to replicate the locomotion characteristics of the frog's musculoskeletal system. By employing a torsional drive mechanism, it releases the elastic potential energy stored in the actuator, enabling the robot to achieve a jump height of 2.5 meters. In 2021, Gao Feng [43] proposed a frog-inspired jumping robot based on explosive propulsion, targeting the high-energy, high-density explosive jumping mechanism of frogs, as shown in figure 3(c). The robot was designed by simplifying the model of the frog's hind and forelimb structures, using explosive propulsion as the actuator, achieving high explosive performance and continuous jumping motion. In 2022, Fan Jizhuang [44] from Harbin Institute of Technology, inspired by the jumping motion of frogs, developed a novel bio-inspired frog jumping robot, as shown in figure 3(d). The robot features a single-degree-of-freedom six-bar linkage hindlimb mechanism, which utilizes an energy storage spring and a triggering mechanism to achieve a maximum jumping height of 250 mm.

 doi:10.20944/preprints202604.2226.v1

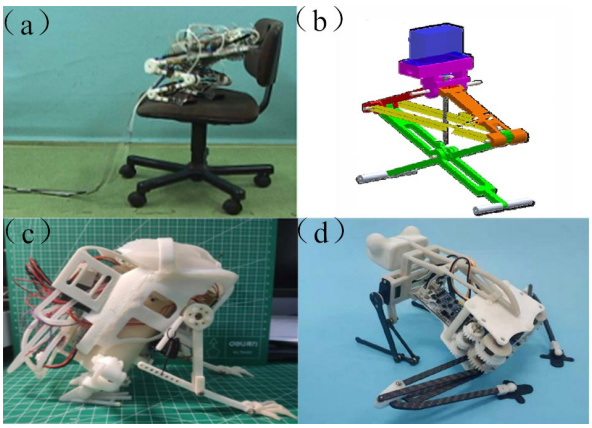

Figure 3. Bio-inspired frog jumping robots:(a) Multi-joint actuated type [41];(b) Elastomer-actuated type [42];(c) Combustion-actuated type [43];(d) Spring energy storage-actuated type [44].

Similarly, many researchers both domestically and internationally have been inspired by the swimming characteristics of frogs and have begun designing various frog-inspired swimming robots based on different drive mechanisms since the early stages. In recent years, related studies have emerged. In 2015, Qiu Yulong [45] from Harbin Institute of Technology, inspired by the biomechanical motion characteristics of frog hindlimbs, developed a frog-inspired swimming robot based on pneumatic muscles, as shown in figure 4(a). The robot employs a mechanism combining pneumatic muscle actuation, wire transmission, and spring-based resetting to achieve frog-style swimming in water. During the propulsion phase, the robot reaches an average velocity of up to 229 mm/s. In 2016, Kong Pengcheng [46] introduced improvements to the previously developed mechanism, as shown in figure 4(b). By optimizing the design of a compact high-pressure air supply system, they enabled the robot to swim autonomously, achieving a propulsion speed of 0.5 m/s. In 2017, Zhang Wei [47] further enhanced the control system based on the aforementioned research, as illustrated in figure 4(c). Inspired by the joint motion patterns of frogs, they designed a controller compatible with pneumatic muscle actuators to precisely control the joint movements, allowing the robot to reach a swimming speed of 790 mm/s in water. In 2017, researchers from the Department of Mechanical Engineering at the National University of Singapore [48] developed a frog-inspired swimming robot driven by dielectric elastomer actuators, as shown in figure 4(d). The robot primarily features a hind-leg mechanism consisting of two joints and two webbed feet. Driven by the dielectric elastomer actuators, the webbed feet perform a complete movement cycle with a duration of 4 seconds, achieving an average swimming speed of 19 mm/s. In the same year, Gul [49] from Jeju National University in South Korea, inspired by the locomotion mechanism of frogs, developed a frog-like soft swimming robot based on shape memory alloys, as shown in figure 4(e). The robot utilizes atomic layer deposition (ALD) technology to integrate flexible sensors into its limbs for real-time angle measurement. By activating the muscle actuators, the robot achieves coordinated movement between the torso and hind limbs, enabling it to perform basic frog-like swimming motions. In summary, although the frog-inspired robot demonstrates good locomotion performance in specific scenarios, it still faces challenges in practical applications, such as slow movement speed, poor adaptability, and limited motion modes, making it difficult to operate effectively in amphibious environments. Moreover, the high manufacturing and material costs of certain technologies hinder its widespread adoption.

 doi:10.20944/preprints202604.2226.v1

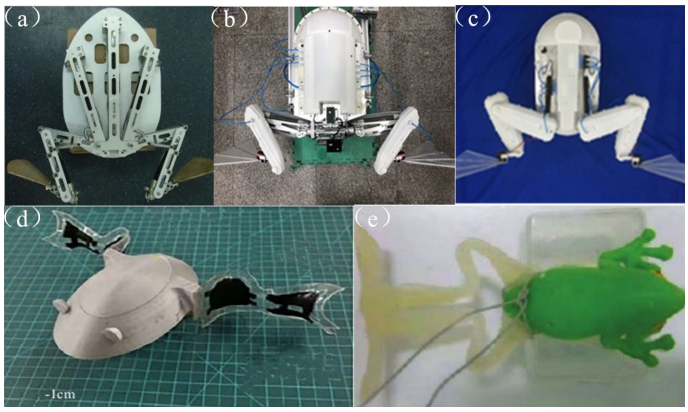

Figure 4. Frog-Inspired Swimming Robots:(a) First-generation robot driven by pneumatic artificial muscles [45]; (b) Second-generation robot driven by pneumatic artificial muscles [46];(c) Third-generation robot driven by pneumatic artificial muscles [47];(d) Robot driven by dielectric elastomer actuators [48];(e) Robot driven by shape memory alloy actuators[49].

Based on the above, existing amphibious robots typically employ a switching structure approach to achieve operation across different media. However, this approach leads to complex structures and still faces numerous challenges in terms of waterproofing and structural maintenance. Additionally, the extra motion switching introduces additional control mechanisms, making control research more challenging. To address the aforementioned issues, inspired by the amphibious locomotion characteristics of biological frogs, this paper proposes a frog-like hybrid-driven amphibious robot. The robot employs a hybrid drive system to achieve amphibious motion, including both frog-like swimming and jumping. On land, a combustion-driven rear limb propulsion mechanism is used, in conjunction with a linkage-based front limb posture adjustment mechanism, to achieve high-performance frog-like jumping. In water, a rope-driven linked rear limb mechanism performs extension and retraction movements, while a controllable soft-bodied extension-driven webbed foot mechanism is employed for oscillation and flexion, enabling efficient frog-like swimming. Compared to other amphibious robots, the robot's drive system adopts a modular design, significantly reducing the complexity of switching between amphibious modes, thereby improving the robot's adaptability and controllability in both terrestrial and aquatic environments.

2. Structural Design of a Frog-Inspired Amphibious Robot

2.1. Structural Modeling Simplification of the Frog-like Amphibious Robot

Frogs live in complex amphibious environments, and with continuous evolution, their biological mechanisms exhibit significant flexibility, resulting in complex movement patterns. Therefore, the robotic mechanism model design has yet to fully replicate the skeletal, muscular, and biomechanical motion characteristics of biological frogs. It is necessary to perform a reasonable abstraction and simplification of the frog's skeletal structure, muscles, and movement characteristics. To enable the robotic mechanism model to achieve the amphibious multi-dimensional movement pattern of the frog, the hip and shoulder joints are simplified as two independently moving joints within a plane. As shown in figure 5(a), based on the analysis of the frog skeletal system for jumping motion, its hind limbs can be simplified into a planar linkage mechanism consisting of the hip joint, knee joint, ankle joint, tarsometatarsal joint, thigh, calf, and hind toes, where the hind toes are simplified from the phalanges and metatarsal bones. However, the forelimb can be regarded as a planar linkage mechanism in the vertical plane, composed of the shoulder joint, elbow joint, upper arm, and forearm. Similarly, as shown in figure 5(c), based on the analysis of the frog skeletal system for swimming motion, its hind limbs can be simplified into a horizontal plane linkage mechanism consisting of the hip joint, knee joint, ankle joint, thigh, calf, and webbed feet, where the webbed feet are simplified from the webbing between the tarsal bones, metatarsal bones, and phalanges. However, the forelimb

 doi:10.20944/preprints202604.2226.v1

can be regarded as a horizontal plane linkage mechanism, composed of the shoulder joint, elbow joint, upper arm, and forearm.

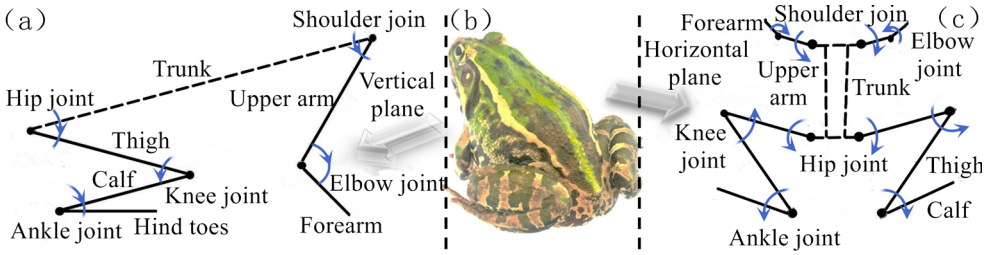

Figure 5. Simplified analysis of frog bone structure: (a) Jumping mechanism; (b) Real frog; (c) Swimming mechanism.

Based on the above amphibious structural modeling of the frog, it can be concluded that when a frog jumps on land, the jump height and distance depend on the explosive force of the hind limbs. The hind limbs release energy through the rapid contraction of muscles, causing the thigh and calf in the hind limb mechanism to quickly extend and align in a straight line, as shown in figure 6. At this moment, the webbed feet of the hind limbs generate a strong reactionary thrust against the ground. Therefore, in response to the high-energy, high-density jumping drive characteristics, thigh, calf, hip joint, and knee joint of the frog's hind limb mechanism during jumping in the vertical plane are equivalent to the linear motion of an explosive drive actuator. This is combined with the ankle joint, hind toes, and forelimb mechanism, which are abstracted into a jumping power mechanism model in the vertical plane. In this model, the ankle joint is referred to as the posture joint. Similarly, during the frog's swimming motion, the swimming speed and distance are also determined by the explosive force of the hind limb muscles. The hind limb mechanism quickly extends the thigh and calf outward, causing the webbed feet to generate a mutual reactionary thrust against the water.

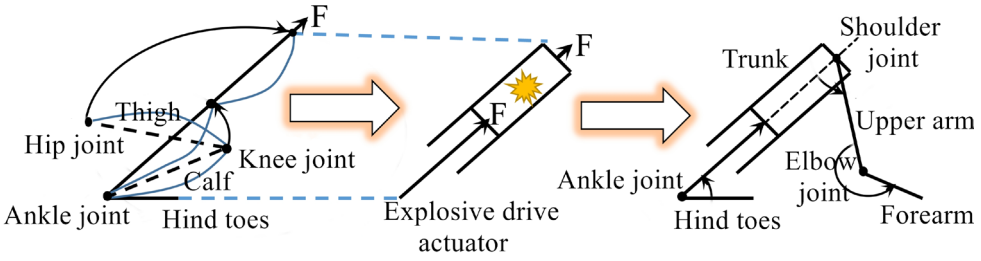

Figure 6. Abstract modeling of the robot's jumping power mechanism.

Therefore, compared to the jumping process, the differences are as follows: First, during swimming, the area of the webbed feet needs to be adjusted, whereas during ground jumping, there is no need to extend the webbed feet. Second, in swimming, the degrees of freedom of the forelimb arm joints and the movement of the elbow joint have a minimal impact on overall acceleration, while during jumping, these joints can adjust the takeoff posture angle and provide cushioning upon landing. Based on the above analysis, in the swimming motion modeling shown in figure 5(c), the forelimb mechanism is omitted, leaving only the hindlimb mechanism. In this mechanism, the hip and knee joints are driven by ropes, while the webbed feet are driven by a controllable extension and swinging mechanism, abstracted as a swimming power mechanism model in the horizontal plane. Finally, by integrating the jumping power mechanism modeling from figure 6, a frog-like hybrid drive amphibious robot structural model is designed, as shown in figure 7.

 doi:10.20944/preprints202604.2226.v1

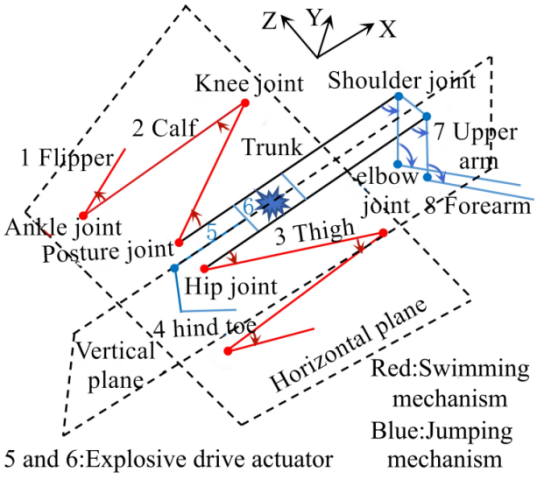

Figure 7. Mechanism model of hybrid drive amphibious robot inspired by frog.

2.2. Design of Frog-Like Jumping Mechanism

Based on the aforementioned amphibian frog-like structural modeling, the robot's jumping mechanism is inspired by the frog's hind limb explosive force and the agile adjustment of its forelimbs during jumping. This mechanism enables the robot to achieve jumping motion on land. It consists of a forelimb mechanism and an explosive actuator. Therefore, for this robot, designing a mechanism capable of mimicking the forelimb functions of a frog is crucial for enhancing its jumping performance and stability. As shown in figure 8, a multi-link mechanism is adopted as the robot's forelimb structure to enable take-off posture adjustment and impact buffering during landing. From the perspective of the frog's biological skeletal structure, the forelimb is small and structurally simple. The forelimb mechanism shown in figure 8 has two degrees of freedom: the active degree of freedom at the shoulder joint and the passive degree of freedom at the elbow joint. Each forelimb mechanism is actuated by a small waterproof servo with a torque of 6 kg·cm. A linkage-driven mechanism is employed, in which the servo directly drives the upper arm to rotate about the shoulder joint, while the forearm is moved through mechanical linkage. Due to the large inertia during landing, it can cause impact damage to the upper arm, forearm, and joint axes. To address this issue, an auxiliary joint 1-2 and an auxiliary forearm are added at the intersection between the forearm and upper arm. This structure not only enhances the coupling motion of the shoulder joint through the auxiliary forearm and joint, but also increases the strength of the forelimb during the landing impact, allowing it to withstand greater forces and reduce damage to the forelimb caused by the interaction with the ground.

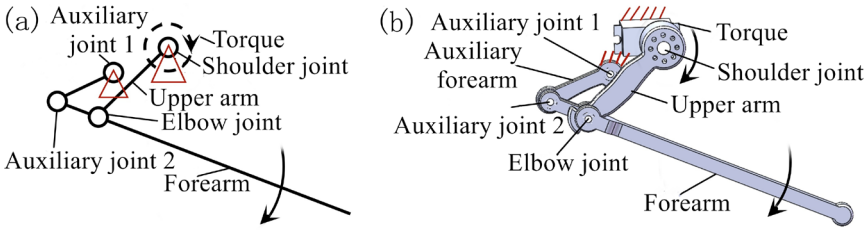

Figure 8. Design of linkage-based forelimb: (a) Sketch of forelimb mechanism; (b) Structure of forelimb mechanism.

Secondly, frogs can generate a powerful explosive force rapidly in the hind limb skeleton due to their muscle tissue, enabling them to achieve high and long jumps. Based on this characteristic, a soft-material elastic and chemically explosive high-density mechanism is employed to design a soft-bodied chamber-based explosive actuator, as shown in figure 9. Its structure consists of an explosive module and a motion module. The explosive module is analogous to the muscle tissue responsible

 doi:10.20944/preprints202604.2226.v1

for generating force in the frog's hind limbs. It consists of an ignition head, a soft-type explosive chamber, and a soft-type explosive chamber cover. The soft-type explosive chamber is the reaction chamber where the explosive reaction occurs. The upper surface of the chamber's inlet is coated with sealing adhesive, which is then bonded to the lower surface of the explosive chamber cover. A hole is located at the center of the soft-material explosive chamber cover, which is connected to the lower surface. The ignition head is bonded to this hole using sealing adhesive. The ignition head is equipped with an ignition electrode, gas inlet, and a pressure sensor. The motion module is analogous to the simplified linear motion output of the frog's hind limb bones during a forceful jump. It consists of a force-driving pushrod and the hind toes. The outer sides of the force-driving pushrod are equipped with convex guide blocks, which allow the pushrod to move in a straight line within the body of trunk along a concave sliding track. Additionally, the force actuator is equipped with a cavity, whose shape and size are consistent with the soft explosive chamber. The soft explosive chamber is embedded within the cavity and is securely attached to the bottom of the force-driving pushrod's inner cavity using a sealing adhesive. When the gas inside the explosive chamber detonates, the force-driving pushrod performs a rapid linear movement outward along the concave sliding groove relative to the body of the robot. Furthermore, torsion springs are embedded on both sides of the hinge between the lower end of the force-driving pushrod and hind toe. The torsion springs serve to quickly restore the hind toe to its original position after the robot completes a jump, utilizing the restoring force of the torsion springs, thus preparing the robot for the next jump.

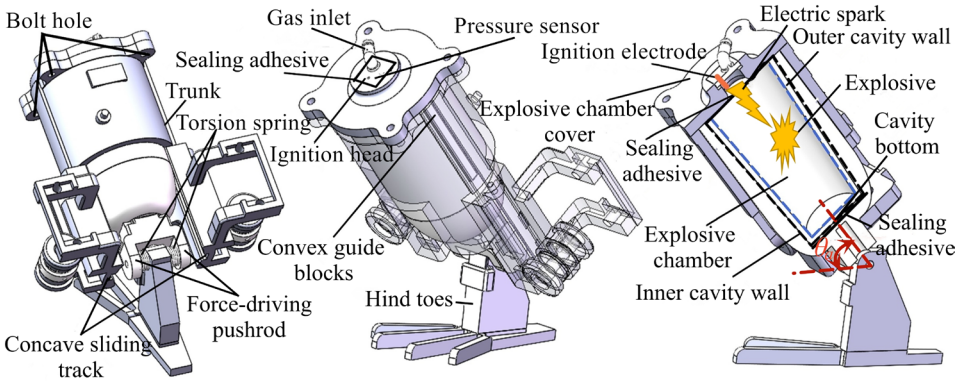

Figure 9. Design of soft-bodied cavity-type explosive actuator.

In summary, the explosive actuator not only enables the robot's trunk to generate a take-off angle when the hind toe contacts the ground under the control of the forelimb mechanism, but also transmits the explosive force generated by the force-driving pushrod through the friction between the hind toe and the ground, thereby generating a reactive force that propels the robot upward. Additionally, once the soft explosive chamber is filled with a hydrogen-oxygen mixture via the pneumatic control system, the main control board immediately activates the ignition system, causing the igniter electrodes to generate an electric spark that triggers combustion of the gas mixture within the chamber. This explosive event drives the explosive actuator to output thrust. Simultaneously, the forelimb mechanism adjusts the takeoff angle between the robot's trunk and hind toes. Under this configuration, the thrust generated by the explosive induces a propulsive force on the hind toes, enabling the robot to perform a frog-like jumping motion.

2.3. Frog-like Swimming Mechanism Design

Based on the amphibious frog-like structure modeling mentioned above, it is understood that the swimming mechanism achieves motion in water through the frog's hind legs extending and retracting, as well as the webbed feet stretching and contracting, mimicking the frog's swimming motion. The mechanism consists of a hind limb propulsion unit and a flipper unit , as shown in figure 10. In this paper, by combining the flexibility of ropes with the rigidity of linkages, a rope-driven

 doi:10.20944/preprints202604.2226.v1

linked hind-leg propulsion mechanism is proposed. Since the initial state of the frog's hind legs during swimming is always in a retracted position, the initial state of the rope-driven linked hind-leg propulsion mechanism is designed to be in a coiled position. The hind-leg propulsion mechanism consists of the thigh, calf, servo motor 1, servo motor 2, rope 1, and rope 2, and is connected to the trunk of the robot through the hip joint and knee joint. The upper end of the flipper mechanism is mounted onto the output shaft of servo 2 at the lower end of the calf, forming the ankle joint. During frog swimming, in addition to the movement of the flippers themselves, the rotational degrees of freedom at the middle joint of the hind limbs need to be controlled. To improve the efficiency of the drive source and reduce weight, the knee joint and hip joint are synchronized and controlled by a single servo motor 1 through a cable linkage (1-2), enabling the synchronized outward/inward swinging degrees of freedom between the thigh and calf. In addition, the flipper mechanism is directly actuated by servo 2 to control its oscillatory motion. In the above design, to reduce weight while ensuring sufficient torque, servos (1-2) are respectively selected as small waterproof servos with torques of 6kg·cm and 4.5kg·cm, with weights of 25g and 15g, respectively. Additionally, to reduce frictional resistance during the relative motion between the hip joint and knee joint, rolling bearings are embedded at both ends inside the joint.

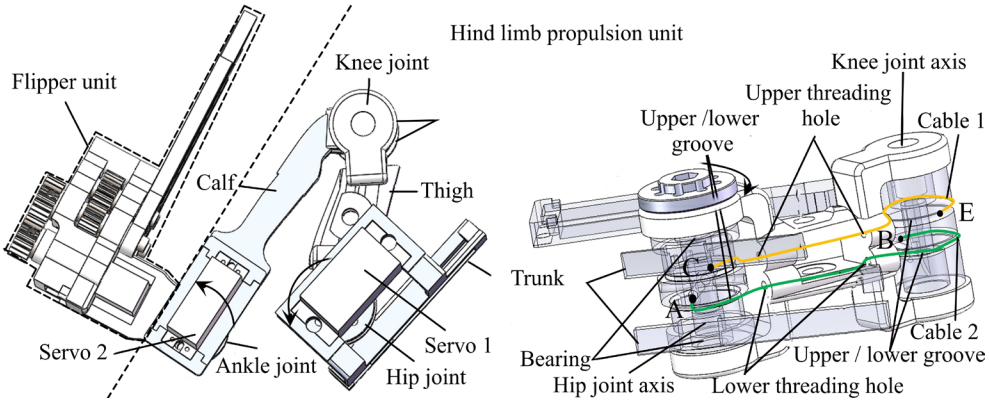

Figure 10. Design of the rope-driven linkage hind limb propulsion mechanism.

When the thigh rotates counterclockwise around the hip joint axis via servo 1, the cable 2 at point A will wind around the hip joint axis within the lower groove of the trunk body. As a result, the front end of the calf at point B will rotate clockwise around the knee joint axis to compensate for the length of the cable wound at the upper end. Meanwhile, cable 1 at point E will simultaneously wind around the knee joint axis within the calf 's front upper groove as the calf rotates clockwise around the knee joint axis. Therefore, the cable at the front end of the thigh at point C will rotate counterclockwise around the hip joint axis to compensate for the length of the cable wound at the upper end. Therefore, cables (1-2) exhibit a closed-loop coupling relationship characterized by equal length motion in opposite directions. Based on this coupling mechanism, as shown in figure 11(a), when servo 1 drives the thigh to rotate counterclockwise around the hip joint, it simultaneously drives the calf to rotate clockwise around the knee joint, resulting in an outward extension of the ankle joint. At this moment, the flipper mechanism expands the surface area of the flipper. As servo 2 subsequently swings counterclockwise around the ankle joint, the propulsion mechanism of the robot generates thrust for swimming motion. Conversely, as shown in figure 11(b), when servo 1 drives the thigh to rotate clockwise around the hip joint, the calf is simultaneously driven to rotate counterclockwise around the knee joint, causing the ankle joint to retract inward. At this stage, the flipper mechanism reduces the flipper surface area. As servo 2 then slowly swings clockwise around the ankle joint, the propulsion mechanism of the robot performs a recovery motion during the swimming cycle.

 doi:10.20944/preprints202604.2226.v1

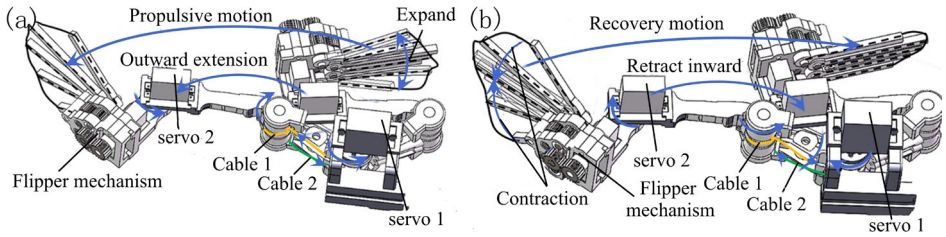

Figure 11. Motion state of the hind limb propulsion mechanism:(a) Outward stretching exercise;(b) Inward curling exercise.

2.4. Body Design of the Frog-Inspired Amphibious Robot

Based on the design of the aforementioned amphibious locomotion mechanism and the integration of the control hardware system, the frog-inspired hybrid-driven amphibious robot proposed in this paper is characterized by its ability to combine jumping and swimming capabilities. The robot employs a hybrid actuation method consisting of cable-driven linkage and combustion-based propulsion, enabling fully autonomous amphibious locomotion over long distances without the need for tethering. The overall modeling structure is illustrated in figure 12, the robot body shown in the figure adopts an overall frog-like design, and is mainly composed of the trunk mechanism, swimming mechanism, jumping mechanism, and control hardware system. The trunk mechanism is primarily composed of the upper shell, lower shell, and the central body. A highly sealed cavity is achieved through a combination of static and dynamic sealing techniques. It serves two main purposes: firstly, to increase its buoyancy through added displacement; secondly, to create a sealed internal compartment functioning as an electronics bay, where the control hardware system is integrated. This configuration enables both housing of the electronic control modules and structural connectivity with the lateral swimming and jumping mechanisms. Consequently, materials selected for the trunk structure and actuation units should exhibit high stiffness and hardness while maintaining a lightweight profile to optimize performance.The swimming mechanism adopts a tendon-driven linkage system to simulate the extension and flexion of frog hindlimb muscles during swimming, enabling coordinated rotation of the hip and knee joints to achieve horizontal propulsion in a breaststroke-like motion. Meanwhile, a servo is integrated at the ankle joint to drive the flipper mechanism, allowing for both swinging motion and flipper opening and closing, Thus enabling frog-like swimming motion underwater. The jumping power mechanism utilizes an explosive combustion-driven system to mimic the powerful burst generated by a frog's hindlimb during jumping. In addition, the forelimbs assist with ground support and jumping angle adjustment during take-off, and provide cushioning during landing, thereby enabling frog-like terrestrial jumping. The control hardware architecture comprises a gas supply module, ignition control board, main controller, pressure sensing unit, and power subsystem. Utilizing a Wireless Communication Module, the host computer transmits control instructions to the embedded controller and receives real-time feedback, enabling accurate regulation of actuator dynamics. Each of the aforementioned modules operates independently while maintaining functional interdependence. Such a design ensures the robot's capability to perform both swimming and jumping in amphibious environments, while also promoting a more compact, lightweight, and agile system architecture.

 doi:10.20944/preprints202604.2226.v1

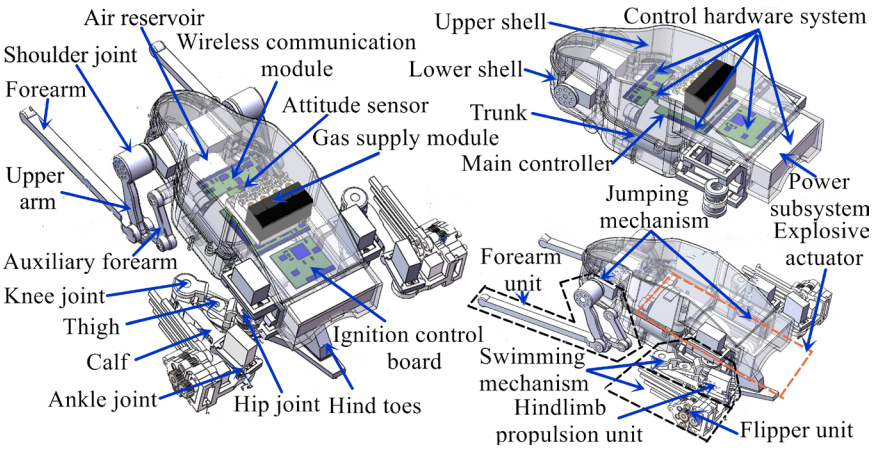

Figure 12. Overall model of hybrid drive amphibious robot inspired by frog.

3. Hybrid Power Modeling of Frog-Inspired Amphibious Robots

3.1. Combustion-Explosion Dynamics Modeling for Robots

During the jumping process of the robot, explosive dynamics refers to the process in which the explosive actuator converts the chemical thermal energy generated by detonation into a reactive force output from the hind toe to the ground. Its simplified mathematical model is shown in figure 13. The trunk, soft explosive chamber, chamber cap, and ignition head are simplified as the upper assembly with a total mass of M1. The force-exerting push rod, and rear toe are simplified as the lower assembly with a total mass of M2. S denotes the motion stroke of the upper assembly relative to the lower assembly; P_0 and P_1 represent the initial pressure and the peak pressure during combustion within the soft combustion chamber, respectively.

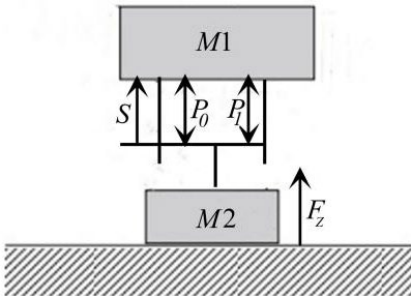

Figure 13. Schematic diagram of detonation dynamics model.

According to the aforementioned combustion-based mathematical model, when the hydrogen-oxygen mixture undergoes detonation, the upper and lower assemblies generate a mutual motion S. By applying Newton's second law, the dynamic equation of the upper assembly during motion S can be expressed as:

$$F_{M1} = (p_1 - p_0) A_q - M1 \cdot g - f \quad (1)$$

where A_p denotes the deformable surface area of the soft actuator chamber (mm²); F_{M1} represents the thrust force of the entire mechanism relative to the hind toe (N); and f is the friction force between the actuation push-rod and the torso body (N).According to Equation (1), the acceleration expression of the upper body during the combustion-driven S-stroke can be derived as follows:

$$a_{M1} = \left[(p_1 - p_0) A_q - M1 \cdot g - f \right] / M1 \quad (2)$$

During combustion-driven motion, the explosive force also actuates the driving pushrod, generating thrust at the hind toe. This results in a balanced state between the hind toe and the ground, and the corresponding dynamic equation is given as:

 doi:10.20944/preprints202604.2226.v1

$$F_{M2} = (p_1 - p_0) A_q - M2 \cdot g - f \quad (3)$$

Due to the vertical contact between the hind toe and the ground, along with its rigidity, the explosive force generates a reaction thrust F_d from the ground. When this reaction force F_d overcomes the total weight of both the upper and lower components, the system can rapidly detach from the ground, enabling a jump with a height H output. By combining Equations (1) and (3), the expression for the output force of the explosive actuator is given as:

$$F_Z = (p_1 - p_0) A_q - (M1 + M2) g - f \quad (4)$$

According to Equation (4), the expression for the acceleration output relative to the ground by the explosive actuator is obtained as:

$$a_d = \left[(p_1 - p_0) A_q - (M1 + M2) g - f \right] / (M1 + M2) \quad (5)$$

As shown in Equation (4), when the mixed gas inside the soft actuator chamber undergoes explosive combustion, the high-energy chemical reaction causes a pressure change within the chamber. This pressure difference, P, directly determines the output performance of the actuator. Since the combustion reaction occurs in a sealed soft actuator chamber, the first law of thermodynamics can be applied as follows:

$$\dot{U}_{(H_2+O_2)} = \dot{Q}_{(H_2+O_2)} - \dot{W}_{(H_2+O_2)} \quad (6)$$

where Q represents the chemical energy released by the combustion of the hydrogen-oxygen mixture, U denotes the internal energy of the gas mixture, and W is the work done by the mixture on the external environment during the explosion process. A mixture of hydrogen and oxygen at a specific ratio is introduced into the soft actuator chamber, where both gases are assumed to behave as ideal gases. The internal energy change of the gas mixture during the combustion process can be expressed as follows:

$$\dot{U}_{(H_2+O_2)} = \frac{\left(\dot{P}V + P\dot{V} \right)}{K_{(H_2+O_2)} - 1} \quad (7)$$

where V denotes the volume of the hydrogen-oxygen mixture injected into the soft actuator chamber (ml), and K represents the adiabatic index of the hydrogen-oxygen gas mixture.The value of K is calculated using the formula $1+R/C^V$, R is the universal gas constant. Assuming complete combustion of hydrogen and oxygen to form H_2O, K is taken as 0.6.The soft chamber is made of flexible silicone material. During the combustion process of the hydrogen-oxygen mixture inside the chamber, work is done accompanied by expansion. The expression for the work done during expansion is as follows:

$$\dot{W}_{(H_2+O_2)} = P\dot{V} \quad (8)$$

Since the mass of the hydrogen-oxygen mixture filled in the chamber is relatively small, the combustion reaction within the soft chamber can be considered as a constant-volume, homogeneous, adiabatic, and complete combustion process. Therefore,. By substituting Equations (8) and (7) into Equation (6), the following expression can be obtained:

$$\dot{P} = -K_{(H_2+O_2)} \frac{P}{V} \dot{V} \quad (9)$$

Further integration of Equation (9) yields the following expression:

$$P_1 = P \left(\frac{V_1}{V_0 + A_q S} \right)^{K_{(H_2+O_2)}} \quad (10)$$

where V_0 is the initial volume of the hydrogen-oxygen mixture charged into the soft actuator chamber. Substituting Equation (10) into Equation (4), the blast-driven dynamic equation can be derived as follows:

 doi:10.20944/preprints202604.2226.v1

$$F_Z = \left(P\left(\frac{V_1}{V_0 + A_q S} \right)^{K_{(H_2+O_2)}} - P_0 \right) A_q - (M1 + M2)g - f \quad (11)$$

3.2. Swimming Dynamics Modeling of the Robot

As shown in figure 14(a), when the robot is in the propulsion phase, the flippers extend outward under the drive of the hind limb propulsion mechanism and spread to contact the water surface for swimming. At this point, the water flow speed behind the flippers increases relative to the water flow in front, generating a thrust in the direction of movement between the flippers and the water, referred to as the propulsive force. During the recovery phase, as shown in figure 14(c), the flippers retract inward under the actuation of the hind limb propulsion mechanism, and the flipper area is reduced while still interacting with the water surface. At this stage, the water flow velocity behind the flippers decreases relative to the front, resulting in a backward-directed force between the flippers and the water, opposite to the swimming direction. This force is referred to as hydrodynamic drag.

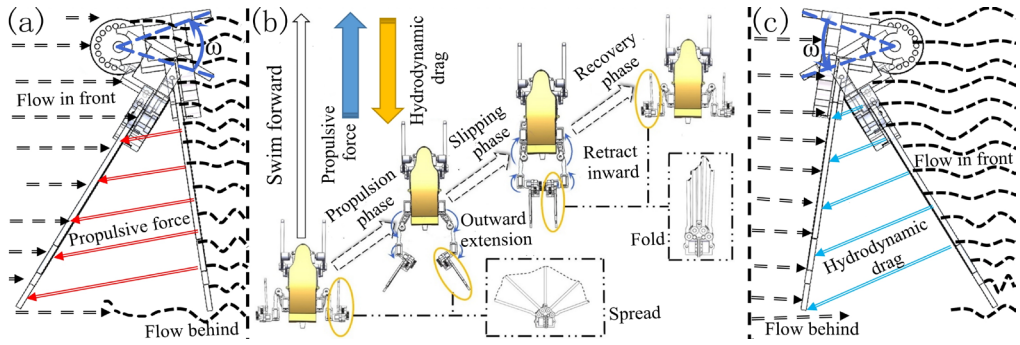

Figure 14. Changes in flippers subjected to water flow field:(a) Propulsion stage;(b) Motion state;(c) Recovery stage.

The robot's side surface of the flippers has a very small width perpendicular to the horizontal plane of the flippers when moving through water, resulting in negligible lift on the side surface, which can be ignored. Considering the motion state generated by the flippers during the stroke, and combining hydrodynamic calculation methods, a hydrodynamic solution formula for the robot was established, as expressed below:

$$F_M = C_D \rho_S \left(S \cdot \sin(\gamma) \right) U_M \left| U_M \right| \quad (12)$$

where ρ_S denotes the density of the water flow, which is 1.0 × 10³kg-m⁻³; S denotes the effective contact area (mm²) between the flippers and the water during the stroke; γ denotes the effective angle between the contact area of the water flow and the flipper surface, ranging from 0°to 180°; C_D denotes the drag coefficient of the flippers during the stroke; U_M is the resultant velocity, combining the propulsion speed V_o of the ankle joint in the base coordinate system and the linear velocity of the flipper at point P. The drag coefficient is determined by the Reynolds number R_n for planar translation and rotation in the fluid flow, where R_n can be expressed as follows in both the laminar and turbulent flow regimes:

$$R_n = \frac{\rho_S \cdot \left| C_D \right| \cdot D}{\zeta} \quad (13)$$

where D is the characteristic length along the direction of the water flow velocity, with the maximum width of the flipper taken as 140 mm; When the fluid velocity is less than 1 m/s, the dynamic viscosity (ζ) of water is 1.01×10⁻³Pa · s. Substituting the relevant parameters into equation （13） to calculate

 doi:10.20944/preprints202604.2226.v1

the Reynolds number, if its value is less than 2*10^5, the drag coefficient is 1.In figure 15(a), the distance between points O_8 and O_9 on the flipper mechanism is very short, so the angular velocity(ω) of point O_9 is approximately equal to the angular velocity of point O_8 . In equation （12）, U_M is the resultant velocity of the ankle joint's propulsion velocity V_o in the base coordinate system and the linear velocity of the flipper at point P. The expression is as follows:

$$U_M = V_o + (\omega \cdot r) \quad (14)$$

As shown in figure15 (b), the area of the flipper in the open position is approximately modeled as a sector with variable area. Using the blade element method, we consider all points on the flipper surface with the same velocity at point P as infinitesimal elements dA, with the rotation radius r as the variable. Then, by integrating equation（12）, the dynamic equation of the robot during swimming is derived. The expression is as follows:

$$\begin{aligned} F_M &= 0.5\int C_D \rho_S U_M |U_M| \sin(\gamma)\, dA \\ &= C_D \rho_S \left(\int_0^c \sin(\gamma) \left(\frac{d-a}{c} n + a \right) (V_o + \omega \cdot r)^2 \, dn \right) \\ &+ C_D \rho_S \left(\int_0^e \sin(\gamma) (V_o + \omega(n + \Delta n))^2 \sqrt{(R)^2 - (b + c + \Delta n)^2}\, d\Delta n \right) \end{aligned} \quad (15)$$

where a, b, c, d, e, and R are all fundamental parameters of the flipper mechanism, with R representing the average length of the flipper's toe bone, which is taken as 52mm. The expressions for the other related fundamental parameters are as follows:

$$\begin{cases} a = b\tan\left(\frac{\theta_z}{2}\right) & c = R\cos\left(\frac{\theta_z}{2}\right) - b \\ d = R\sin\left(\frac{\theta_z}{2}\right) & e = R - b - c \end{cases} \quad (16)$$

By solving the above equation （15）, the thrust and hydrodynamic drag forces during the propulsion and recovery phases of the robot can be calculated with relatively low computational cost. Furthermore, by combining the robot's swimming kinematic equations, it is possible to analytically determine the variation in hydrodynamic forces throughout the entire cycle, providing the foundation for subsequent trajectory planning and optimization.

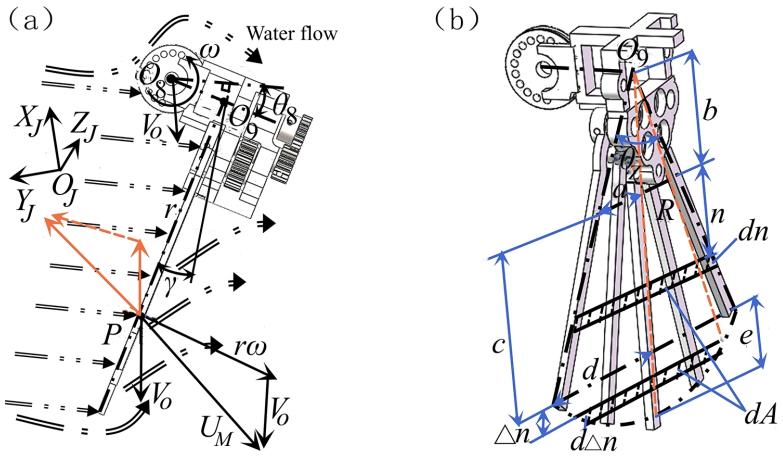

Figure 15. Force model of flipper motion in water:(a) Force analysis of flipper motion; (b) Basic parameters of flipper.

 doi:10.20944/preprints202604.2226.v1

4. Analysis of the Movement Capabilities in Frog-like Amphibious Robots

4.1. Frog-Style Jumping Motion

As shown in figure16(a), the proposed jumping mechanism in this paper indicates that during the jumping process, the takeoff posture is determined by the horizontal angle θ_a between the force-driving pushrod in the explosive drive unit and the hind toe. The takeoff posture angle is adjusted by the forelimb mechanism, which regulates the vertical distance between the robot's centerline and the ground's horizontal plane.The overall structure of the robot is symmetrically distributed. The coordinate system is established for the unilateral forelimb mechanism, as shown in figure 16(b).

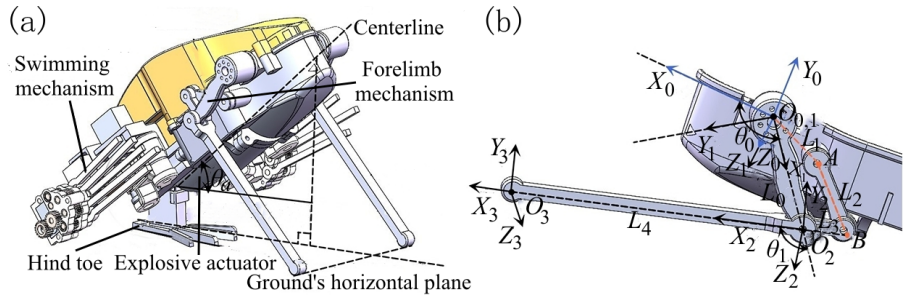

Figure 16. Robot jumping mode diagram:(a) Robot posture angle;(b) Coordinate system.

According to the right-hand rule, coordinate systems O_0-$X_0Y_0Y_0$ and O_1-$X_1Y_1Y_1$ are established at the shoulder joint, the coordinate system O_2-$X_2Y_2Y_2$ is established at the elbow joint, and the coordinate system O_3-$X_3Y_3Y_3$ is established at the distal end of the forearm. Based on the link transformation matrix method, the D-H parameter table 1.1 for the left forelimb mechanism is obtained.

Table 1.1. D-H parameter table of the robot's left forelimb.

Joint Number（i）	α_{i-1}（◦）	a_{i-1}（mm）	d_i（mm）	θ_{i-1}（◦）	Angle
1	0	0	0	θ_0	80˚-130˚
2	0	L_0=47	0	θ_1	-40˚-90˚
3	0	L_4=125	0	0	0

Based on the transformation matrix ${}^{i-1}_{i}T$ between adjacent joint generalized coordinate systems, the general form is:

$$ {}^{i-1}_{i}\boldsymbol{T} = \begin{bmatrix} c\theta_i & -s\theta_i & 0 & a_{i-1} \\ s\theta_i c\alpha_{i-1} & c\theta_i c\alpha_{i-1} & -s\alpha_{i-1} & -d_i s\alpha_{i-1} \\ s\theta_i s\alpha_{i-1} & c\theta_i s\alpha_{i-1} & c\alpha_{i-1} & d_i c\alpha_{i-1} \\ 0 & 0 & 0 & 1 \end{bmatrix} \quad (17) $$

In the equation, c represents cos, s represents sin, and i denotes the i-th coordinate frame. Based on equation (17) and the link parameters shown in Table 1-1, by multiplying the transformation matrices of each link, the transformation matrix of the forearm end-effector coordinate frame O_3-$X_3Y_3Z_3$ relative to the base coordinate frame O_0-$X_0Y_0Z_0$ can be obtained as follows:

$$ {}^{0}_{3}\boldsymbol{T} = {}^{0}_{1}\boldsymbol{T}\left(\theta_0\right) \cdot {}^{1}_{2}\boldsymbol{T}\left(\theta_1\right) \cdot {}^{2}_{3}\boldsymbol{T}\left(0\right) \quad (18) $$

In further rearranging Equation（18）, the kinematic equation of the forearm end point in the left forelimb mechanism relative to the base coordinate frame of the shoulder joint, O_0-$X_0Y_0Y_0$, can be obtained as:

 doi:10.20944/preprints202604.2226.v1

$$\begin{bmatrix} X_{3,0} \\ Y_{3,0} \\ Z_{3,0} \end{bmatrix} = \begin{bmatrix} L_4 \cdot \cos(\theta_0 + \theta_1) + L_0 \cdot \cos(\theta_0) \\ L_4 \cdot \sin(\theta_0 + \theta_1) + L_0 \cdot \sin(\theta_0) \\ 0 \end{bmatrix} \quad (19)$$

where $(X_{3,0}, Y_{3,0}, Z_{3,0})^T$ represents the position vector, and $Y_{3,0}$ is the motion equation of the forearm end point O_3, which is the distance in the Y-direction perpendicular to the ground. The forelimb mechanism adopts a multi-link design. Driven by the upper arm, the upper end point B of the forearm is constrained by the auxiliary forearm through a pulling mechanism, enabling the upper end of the forearm to swing forward and backward with the upper arm around the elbow joint O_2. Therefore, a certain coupled motion relationship exists between the driving angles θ_1 and θ_0, as illustrated in figure17(a~b).

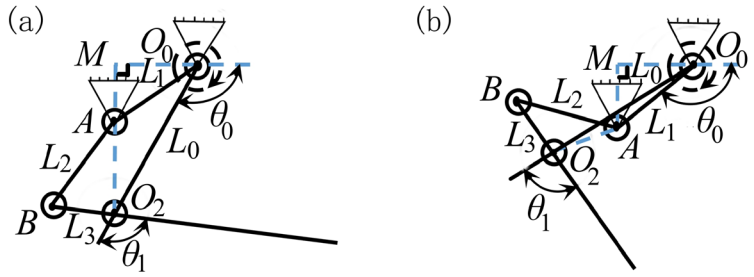

Figure 17. Schematic diagram of the forelimb mechanism motion: (a) Does not exceed line segment AO_0; (b) Exceeds the line segment AO_0.

As shown in figure17(a), when the upper arm rotates clockwise but does not exceed the position of segment AO_0, the three sides of right triangle $\triangle AMO_0$ are known, enabling the calculation of angle $\angle MO_0A$ via inverse kinematics. Given the driving angle of the upper arm θ_0, angle $\angle AO_0O_2$ can be further derived. The analytical expressions are as follows:

$$\angle AO_0O_2 = 180^\circ - \left(\theta_0 + \arccos\left(\frac{MO_0}{L_1} \right) \right) \quad (20)$$

In the equation, the value of θ_0 is in the range $[0^\circ, 40^\circ]$.Given triangle $\triangle AO_0O_2$ with two known sides and the included angle $\angle AO_0O_2$, the law of cosines is applied to derive the equation for the varying length of segment AO_2 during motion, as well as the angle $\angle AO_2O_0$. The expressions are as follows:

$$\begin{cases} AO_2 = \sqrt{(L_1)^2 + (L_0)^2 - 2L_1L_0 \cos \angle AO_0O_2} \\ \angle AO_2O_0 = \arccos\left(\dfrac{(AO_2)^2 + (L_0)^2 - (L_1)^2}{2AO_2L_0} \right) \end{cases} \quad (21)$$

Similarly, given triangle $\triangle ABO_2$ with all three sides known, the law of cosines in conjunction with equation (21) is applied to derive the motion equation for the varying angle $\angle BO_2A$. The expression is as follows:

$$\angle BO_2A = \arccos\left(\frac{(AO_2)^2 + (L_3)^2 - (L_2)^2}{2AO_2L_3} \right) \quad (22)$$

By summing the included angles derived from equations (21) and (22), the mapping function of the elbow joint angle θ_1 with respect to the input angle θ_0 can be further obtained. The resulting expression is as follows:

$$\theta_1 = \angle AO_2O_0 + \angle BO_2A \qquad 0^\circ \le \theta_0 \le 40^\circ \quad (23)$$

 doi:10.20944/preprints202604.2226.v1

As shown in figure17(b), when the upper arm rotates clockwise past the position of segment AO_0, the angle $\angle AO_0O_2$ can be determined based on the known angle $\angle MO_0A$ and the input angle θ_0 of the upper arm. The expression is given as follows:

$$\angle AO_0O_2 = \theta_0 - \left(180^\circ - \arccos\left(\frac{MO_0}{L_1}\right)\right) \quad (24)$$

In the equation, the value of θ_0 is in the range [40°, 90°]. By substituting Equation （24） into Equation （21）, the motion length change equation for segment AO_2 and the angle $\angle AO_2O_0$ can be determined. Through the application of the motion variation equation of angle $\angle BO_2A$ from Equation （22） and performing a subtraction operation, the motion variation equation of the elbow joint angle θ_1 in relation to the input angle θ_0 can be obtained, as follows:

$$\theta_1 = \angle BO_2A - \angle AO_2O_0 \qquad 40^\circ \le \theta_0 \le 90^\circ \quad (25)$$

By combining Equations （23） and （25）, the kinematic equation relating the driving angle θ_0 and the elbow joint angle θ_1 of the forelimb mechanism throughout the entire motion process can be derived as follows:

$$\theta_1 = \begin{cases} \angle BO_2A + \angle AO_2O_0 & 0^\circ \le \theta_0 \le 40^\circ \\ \angle BO_2A - \angle AO_2O_0 & 40^\circ \le \theta_0 \le 90^\circ \end{cases} \quad (26)$$

It can be seen from Equation （26） that L_0, L_1, L_2, L_3, and M_0 are predetermined design constants, with θ_0 being the sole variable parameter affecting the mechanism. Therefore, it can be further simplified as $\theta_1 = C{\cdot}\theta_0$, where C represents the functional relationship defined in Equation （26）. Based on the calculation from Equation （19）, the kinematic model of the forearm end-effector with respect to the driving angle is obtained as follows:

$$\begin{bmatrix} X_{3,0} \\ Y_{3,0} \\ Z_{3,0} \end{bmatrix} = \begin{bmatrix} L_4 \cdot \cos\left(\theta_0\left(1+C\right)\right) + L_0 \cdot \cos\left(\theta_0\right) \\ L_4 \cdot \sin\left(\theta_0\left(1+C\right)\right) + L_0 \cdot \sin\left(\theta_0\right) \\ 0 \end{bmatrix} \quad （27）$$

Based on the previously established model of the robot's jumping actuation mechanism, the schematic diagram of the robot's jumping motion was drawn, including the take-off posture angle and the jumping trajectory, as shown in figure 18(a~b).

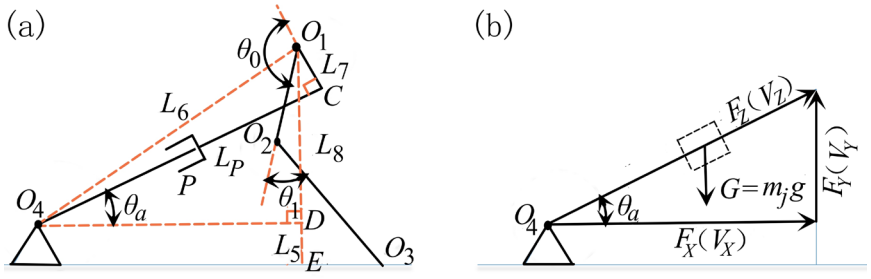

Figure 18. Schematic diagram of the robot's jumping motion principle：(a) Take-off posture angle;(b)Jumping movement.

According to the kinematic equations of the forearm end-effector derived above, the displacement $Y_{3,0}$ of point O_3 along the Y-axis determines the variation in the robot's take-off posture angle.Given the right triangle $\triangle O_4CO_1$ in figure 18(a), where the side lengths L_P and L_7 are known, the length of side L_6can be derived using the Pythagorean theorem as follows:

$$L_6 = \sqrt{\left(L_p\right)^2 + \left(L_7\right)^2} \quad (28)$$

Referring to the right triangle $\triangle O_4CO_1$ in the figure, the included angle between the sides L6 and L7 can be determined.

 doi:10.20944/preprints202604.2226.v1

$$\angle O_1O_4C = \arcsin\left(L_7 \Big/ \sqrt{\left(L_p\right)^2 + \left(L_7\right)^2} \right) \quad (29)$$

Similarly, based on the right triangle △O_4DO_1 in the figure, the included angle between sides L6 and L8 can be calculated.

$$\angle O_1O_4D = \arcsin\left(L_8 \Big/ \sqrt{\left(L_p\right)^2 + \left(L_7\right)^2} \right) \quad (30)$$

Given that the vertical motion equation of point O_1 on the Y-axis is known, the length of O_1E is Y_{3-0}. Also, since the length of DE is L_5, substituting into equation （30） allows further calculation of:

$$\angle O_1O_4D = \arcsin\left(\frac{Y_{3-0} - L_5}{\sqrt{\left(L_p\right)^2 + \left(L_7\right)^2}} \right) \quad (31)$$

By combining equations （30） and （29）, the motion equation for the robot's take-off posture angle is obtained, expressed as follows:

$$\theta_a = \arcsin\left(\frac{Y_{3-0} - L_5}{\sqrt{\left(L_p\right)^2 + \left(L_7\right)^2}} \right) - \arcsin\left(\frac{L_7}{\sqrt{\left(L_p\right)^2 + \left(L_7\right)^2}} \right) \quad (32)$$

The lengths of L_5, L_7, and L_p are fixed values based on the prototype dimensions. Under the adjustment of the robot's take-off posture angle, and in conjunction with the explosive dynamics equation （11） in Section 3.1.1, a frog-like jumping motion on land is achieved, as illustrated in figure 18(b). Given the driving force F_Z from the explosive actuator on the robot's rear toe, and applying the laws of energy and momentum conservation, the maximum initial velocity and total work of the robot during the explosive jump are determined：

$$\begin{cases} V_z = \left(F_Z / m_j\right) \cdot T_0 \\ W_z = \left(m_j \cdot \left(V_z\right)^2 / 2\right) \end{cases} \quad (33)$$

where m_j is the total mass of the robot (g), and T_0 is the duration of the explosive actuation (s). During the robot's jumping process, the explosive actuation occurs over an extremely short duration, approximately 0.2 ms. The jump is modeled as a projectile motion and is analyzed by decomposing it into vertical and horizontal components. Using Equations （32） and （27）, the initial values of the horizontal and vertical velocities V_X and V_Y are derived：

$$\begin{cases} V_X = \cos\left(\theta_a\right) \cdot V_z \\ V_Y = \sin\left(\theta_a\right) \cdot V_z \end{cases} \quad (34)$$

The vertical velocity V_Y undergoes uniform deceleration due to gravity until it reaches zero. During this time interval T_1, the upward vertical displacement can be approximated as the jump height, where $T_1 = V_Y/g$. By combining the equations of velocity and displacement, the motion equation for the robot's jump height is derived as follows:

$$H = \left(2V_Y \sin\left(\theta_a\right)V_z - \left(V_Y\right)^2\right) \Big/ 2g \quad (35)$$

When the robot reaches the maximum jump height H, it begins to fall to the ground under the influence of its own weight. The corresponding landing time can be calculated as follows:

$$T_2 = \left(\sin\left(\theta_a\right)V_z - \cos\left(\theta_a\right)V_Y\right) \Big/ g \quad (36)$$

From takeoff to landing, the robot's horizontal velocity component V_X remains constant. The total time is $T_3 = T_1 + T_2$. By combining the velocity and displacement equations, the robot's jump distance motion equation is derived as follows:

 doi:10.20944/preprints202604.2226.v1

$$L_Y = \sin(2\theta_a) V_z^2 / 2g \quad (37)$$

4.2. Frog-Style Swimming Motion

When the robot swims through the propulsion mechanism in water, the thigh, calf, and fin parts of the hind limb propulsion mechanism are simplified as a three-link hind limb mechanism model in the horizontal plane, as shown in figure 19. The robot's swimming mechanism is symmetrical, and the motion analysis is performed on its left side. The robot's center of mass reference frame O_a-$X_aY_aZ_a$ moves in the world coordinate system O_J-$X_JY_JZ_J$. Using the right-hand rule, the coordinate frames O_6-$X_6Y_6Z_6$, O_7-$X_7Y_7Z_7$, O_8-$X_8Y_8Z_8$, and O_{10}-$X_{10}Y_{10}Z_{10}$ are established at the hip joint, knee joint, ankle joint, and the end of the footweb in the hind limb mechanism, respectively. For computational convenience, several auxiliary coordinate frames have been added, namely O_4-$X_4Y_4Z_4$, O_5-$X_5Y_5Z_5$, and O_9-$X_9Y_9Z_9$.

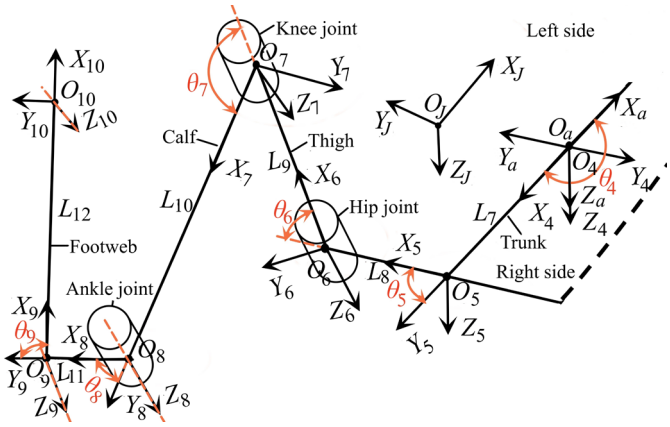

Figure 19. Kinematic model of robot swimming.

Based on the joint coordinate frames shown in figure 19, and using the D-H parameter method, the parameter table for the robot's left hind limb mechanism (Table 1.2) is obtained, with the following data:

Table 1.2. D-H parameters of the left hindlimb mechanism of the robot.

Joint Number（i）	α_{i-1}（°）	a_{i-1}（mm）	d_i（mm）	θ_i（°）	Angle
4	0	0	0	θ_4	-180°
5	0	L_7=63	0	θ_5	-90°
6	0	L_8=42	0	θ_6	-50°~70°
7	0	L_9=45	0	θ_7	0°~150°
8	0	L_{10}=65	0	θ_8	-80°~80°
9	0	L_{11}=21	0	θ_9	-90°
10	0	L_{12}=65	0	0	0°

Based on the coordinate transformation matrices in Equation（17）, the parameters from Table 1.2 are substituted into the calculations to obtain the transformation matrix. Then, by multiplying the transformation matrices, the transformation matrix of the hind limb footweb end relative to the base coordinate frame O_a-$X_aY_aZ_a$ is obtained:

$$ {}^{a}_{10}\boldsymbol{T} = {}^{a}_{4}\boldsymbol{T} \cdot {}^{4}_{5}\boldsymbol{T} \cdot {}^{5}_{6}\boldsymbol{T} \cdot {}^{6}_{7}\boldsymbol{T} \cdot {}^{7}_{8}\boldsymbol{T} \cdot {}^{8}_{9}\boldsymbol{T} \cdot {}^{9}_{10}\boldsymbol{T} \quad (38)$$

where it represents the transformation matrix of the hind limb mechanism in the world coordinate system O_J-$X_JY_JZ_J$, with the end coordinate frame O_{10}-$X_{10}Y_{10}Z_{10}$ relative to the base coordinate frame

 doi:10.20944/preprints202604.2226.v1

O_a-$X_aY_aZ_a$. By simplifying and calculating Equation （38）, the motion equation for the footweb end of the robot's hind limb mechanism is obtained, with the following expression(X_{a-10},Y_{a-10},Z_{a-10}):

$$ {}^{a}_{10}\boldsymbol{T} = \begin{bmatrix} X_{a-10} \\ Y_{a-10} \\ Z_{a-10} \end{bmatrix} = \begin{bmatrix} L_{10}S_{67} - L_7 + L_9S_6 + L_{12}C_{678} + L_{11}S_{678} \\ L_{12}S_{678} - L_{10}C_{67} - L_9C_6 - L_{11}C_{678} - L_8 \\ 0 \end{bmatrix} \quad (39) $$

where C_6 represents cos(θ_6); C_{67} represents cos(θ_6+θ_7); C_{678} represents cos(θ_6+θ_7+θ_8); S_{67} represents sin(θ_6+θ_7); and S_{678} represents sin(θ_6+θ_7+θ_8). As shown in figure 20 (a~b), due to the rope-driven linkage motion mechanism employed in the robot's hind limb mechanism, which includes the hip joint, knee joint, thigh, and lower leg, there exists a coupling relationship between the input of the hip joint angle and the output of the knee joint.

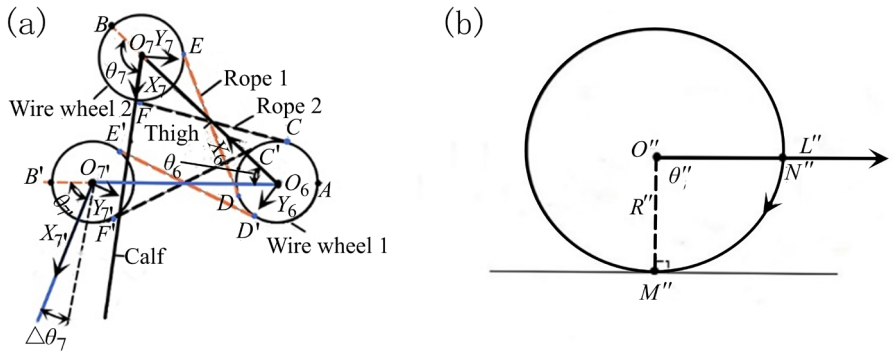

Figure 20. Movement relationship of the robot's hind limb:(a)Principle of rope-driven coupled motion;(b)Principle of circular rolling.

Given that in figure 20 (b), the circle O'' rolls clockwise from point N'' to point M'' by an angle θ'', the arc length L'' of the forward movement of the center of circle O'' is obtained as follows:

$$ L'' = 2R''\pi\theta/360^\circ \quad (40) $$

As shown in figure 20 (a), when the thigh O_6O_7 rotates counterclockwise by an angle θ_6 around point O_6 as the center, the wire wheel 1 also rotates counterclockwise by an angle θ_6 around point O_6 with a radius R1. The value of ΔH is obtained according to the above formula （40）:

$$ \Delta H = 2\theta_6 R_1\pi/360^\circ \quad (41) $$

Since the length of DB on rope 1 is shortened by ΔH, the endpoint B of the wire wheel 2 on the lower leg will be pulled by rope 1 to point B', and will rotate clockwise around point O_7 with a radius R_2 by an angle $\Delta\theta_7$. The rotation angle is calculated according to formula （41）:

$$ \Delta\theta_7 = \Delta H \cdot 360^\circ/(2\pi R_2) \quad (42) $$

By substituting formula (41) into formula (42), the result is obtained as follows:

$$ \Delta\theta_7 = \theta_6 R_1/R_2 \quad (43) $$

Since the initial angle of the lower leg mechanism is θ_7, after the angular change described by formula (43), the resulting changed angle is obtained as follows:

$$ \theta_{7'} = \theta_7 - \Delta\theta_7 \quad (44) $$

By substituting formulab (43) into formula(44), the kinematic geometric relationship expression between the knee joint angle output and the hip joint angle input is further obtained as follows:

$$ \theta_{7'} = \left[\theta_7 - \left[\frac{\theta_6 \cdot R_1}{R_2}\right]\right] \quad (45) $$

 doi:10.20944/preprints202604.2226.v1

By substituting the mapped kinematic relationship from formula (45) into formula (39) ${}^{a}_{10}\boldsymbol{T}$, the kinematic equation of the robot's end-effector motion under the rear leg mechanism drive is further derived as follows:

$$ {}^{a}_{10}\boldsymbol{T}\left(\theta_6,\theta_8\right)=\left[X_{a-10},\ X_{a-10},\ Z_{a-10}\right]^{T} \quad (46) $$

The motion velocity of the ankle joint O_8 in the rear leg mechanism is one of the factors influencing the robot's propulsion and swimming dynamics in the subsequent hydrodynamic calculations. The propulsion motion equation of the ankle joint can be derived from formula (46), and the expression is as follows:

$$ \begin{cases} X_{a-8}=L_{10}\sin\left(\theta_6\left(1+C_7\right)\right)-L_7+L_9\sin\left(\theta_6\right) \\ Y_{a-8}=L_8-L_{10}\cos\left(\theta_6\left(1+C_7\right)\right)-L_9\cos\left(\theta_6\right) \\ Z_{a-8}=0 \end{cases} \quad (47) $$

where C_7 represents the mapping kinematic relationship function of knee joint θ_7, which is output by the hip joint linkage. By applying the time derivative method, the time derivative of the ankle joint motion equation (47) is taken, resulting in the propulsion velocity motion equation of the robot's driven flipper mechanism:

$$ \begin{bmatrix} \dot{X}_{a-8} \\ \dot{Y}_{a-8} \end{bmatrix}=\begin{bmatrix} L_9\cos\left(\theta_6\right)+L_{10}\cos\left(\theta_6+C_7\right) & L_{10}\cos\left(\theta_6+C_7\right) \\ L_9\sin\theta_6+L_{10}\sin\left(\theta_6+C_7\right) & L_{10}\sin\left(\theta_6+C_7\right) \end{bmatrix}\begin{bmatrix} \dot{\theta}_6 \\ \dot{C}_7 \end{bmatrix} \quad (48) $$

4. Experiment and Results

4.1. Prototype Hardware Control System

To enable the robot to execute movements according to the set tasks through the control program, as shown in figure 21, the hardware architecture of the system body is constructed. Its hardware architecture includes the main control board, host computer, servos, ignition device, gas delivery system, attitude sensors, power supply, and step-down module, among others. The robot in this paper primarily integrates an independent ignition control hardware system, a pneumatic control hardware system, an electronic control hardware system, a wireless data transmission control hardware system, and a power supply control hardware system. The ignition control hardware system and the pneumatic control hardware system are responsible for controlling the explosive drive mechanism in the jumping propulsion system. They mainly consist of the gas delivery system and the ignition device. The electronic control hardware system is responsible for controlling the front limb mechanism, the hind limb propulsion mechanism in the swimming drive system, and the fin mechanism. It primarily consists of servos and servo drivers. The wireless data transmission control hardware system manages data communication between the host computer and the main control board. It primarily consists of a wireless transmission module. The power supply control hardware system primarily provides power to the main control board, ignition control hardware system, pneumatic control hardware system, and electronic control hardware system. It mainly consists of a power supply and a voltage regulation module.

 doi:10.20944/preprints202604.2226.v1

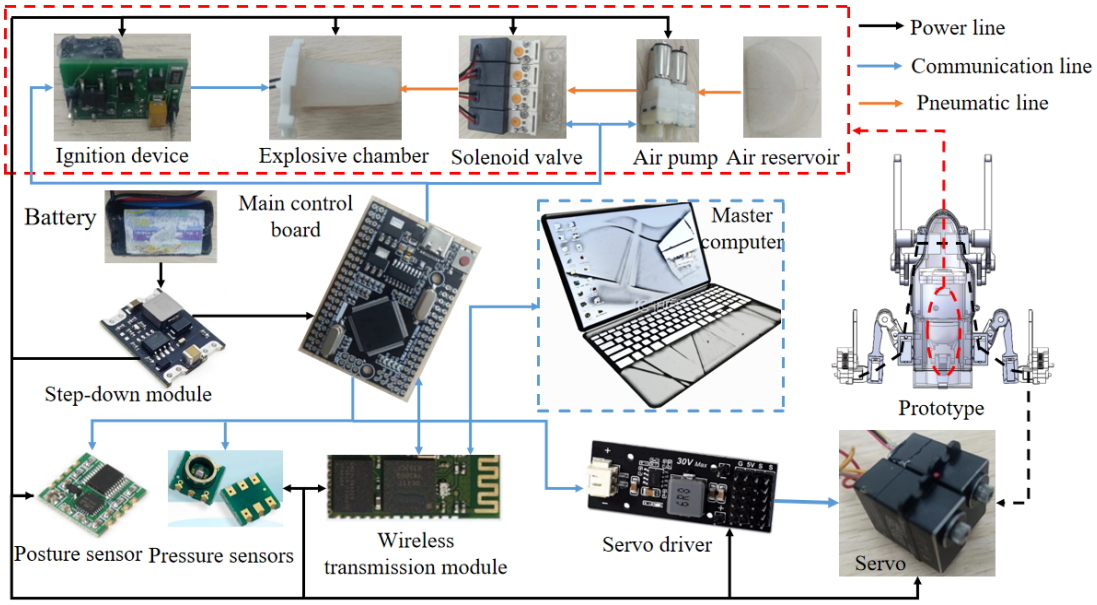

Figure 21. Hardware platform of the robot control system.

In summary, the control mainboard requires a large number of ports, support for adjustable pulse width frequency, and strong computational capabilities. Therefore, the ATmega 2560 was chosen as the main control board. The main control board can fully meet the requirements of the robot's control hardware system. It not only powers itself through the 5V power interface but also outputs 5V and 3V voltages to external components. Additionally, it features 54 digital I/O ports, with 14 of them providing PWM output. This ensures sufficient I/O interfaces for servos, solenoid valves, and air pumps. It also includes 16 analog inputs and outputs, meeting the control requirements for pressure sensors, posture sensor, and ignition devices. Additionally, it is equipped with four TTL serial ports, fully supporting multiple wireless Bluetooth data transmissions. In addition, the battery, step-down module, wireless transmission module, waterproof servo with a torque of 6kg/cm, 8-channel servo driver, and 9-axis posture sensor shown in the diagram all use standardized integrated circuit components, which are capable of meeting the requirements of the robot's drive control system discussed in this paper.Based on the aforementioned hardware control system and the robot structure design discussed in Section 2, a prototype test platform has been built, as shown in figure 22 (a~c).

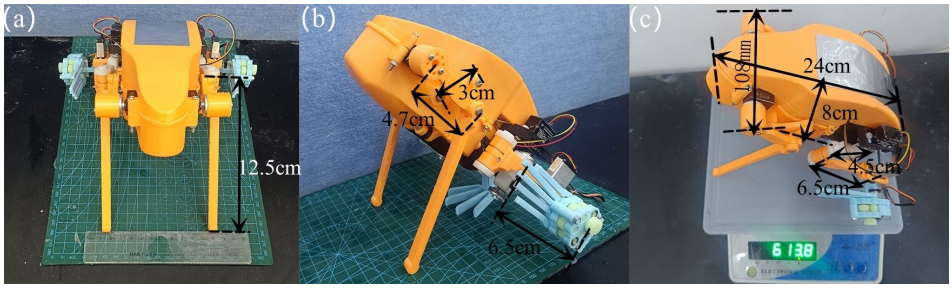

Figure 22. Overall physical prototype of the robot：(a) Front view；(b) Side view;(c) Top view.

The actual dimensions of the robot's front limbs are as follows: upper arm length 47mm, lower arm length 125mm, and auxiliary lower arm length 30mm. The actual dimensions of the robot's hind limbs are as follows: thigh length 45mm, lower leg length 65mm, and foot paddle length 65mm. To provide sufficient drive space for the combustion actuator, two-thirds of the torso length is allocated for the actuator space. The remaining portion, along with the space formed by the upper and lower

 doi:10.20944/preprints202604.2226.v1

housings, is used to house the electrical control hardware. Additionally, the head is designed to accommodate an 80ml air storage tank. Therefore, the overall dimensions of the robot in its initial state are as follows: torso length 240mm, shoulder width 108mm, torso height 95mm, and the total mass is approximately 0.613kg.

4.2. Prototype Frog-Style Swimming Test

According to Chapter 3.2 and 4.2, the extension movement of the propulsion mechanism plays a decisive role in the robot's swimming performance in water. The physical state of the propulsion mechanism on the robot prototype is shown in figure 23 (a~b), with a fully extended length of 175mm. The robot's structure is more compact and lightweight.

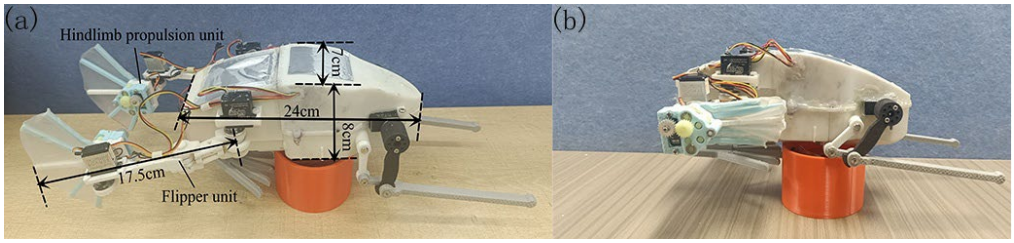

Figure 23. Layout of swimming power mechanism:(a) Stretch state;(b)Crouching state.

The frog's swimming motion in water can be divided into three phases: propulsion, gliding, and recovery. Based on a host computer control program, the swimming actuation mechanism is regulated to enable the robot to perform frog-like swimming experiments in an aquatic environment. After processing the experimental video (**See video 1**) and capturing screenshots, a sequence diagram of the robot's swimming posture was obtained, as shown in figure 24. In the figure, the 'Start' marker indicates the robot's initial position, while the 'End' marker represents the robot's final swimming position. In figure 24(a), the robot achieves straight-line swimming throughout the cycle by actuating only the lateral flippers with an angular velocity of 1.7 rad/s. The flipper opening angle is set at 120 degrees, resulting in a straight swimming distance equivalent to 1.8 times the body length of the prototype, approximately 440 mm, with an average speed of about 73 mm/s.

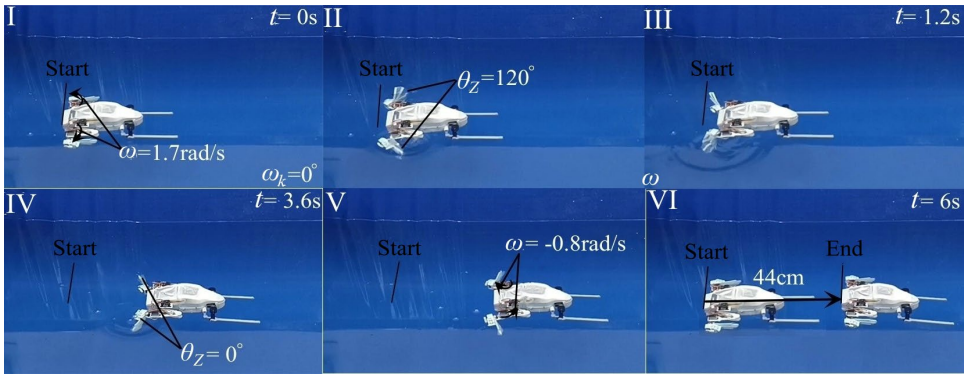

(a) Powered only by flipper

 doi:10.20944/preprints202604.2226.v1

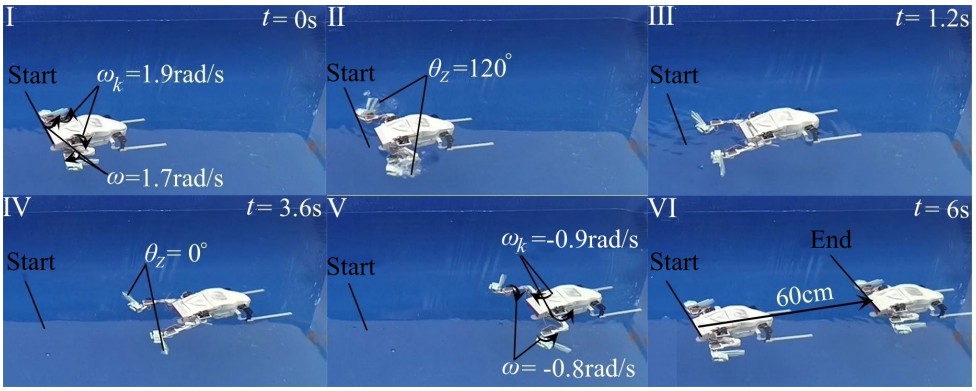

(b) Based on hind limb propulsion mechanism drive

Figure 24. Robot swimming ability test experiment.

Figure 24(b) builds upon the control scheme in figure 24(a) by additionally actuating the hip joints of the posterior limb propulsion mechanism at an angular velocity of 1.9 rad/s. This enhancement extends the straight-line swimming distance to 2.5 times the body length of the prototype, approximately 600 mm, with an average swimming speed of about 100 mm/s. By integrating the acceleration data obtained from the inertial measurement unit (IMU) during the experimental procedure, and applying the physical relationship between force and acceleration, the propulsive force generated by the robot during the propulsion phase in water was experimentally estimated.

At the same time, the theoretical propulsive force was calculated using the hydrodynamic equation （15）, and the results were plotted as shown in figure 25(a~b). As shown in figure 25, when the robot swims in water using only the flipper mechanism, the maximum generated thrust is approximately 22 N. However, when the hind-limb propulsion mechanism is added, the maximum thrust during swimming increases to about 30 N. It can be concluded that the robot increases the line speed of the paddle in the water through the extension motion of the hindlimb propulsion mechanism, thereby further enhancing the robot's propulsion force during swimming. The results above validate the excellent swimming capability of the robot proposed in this paper. Furthermore, the experimental data and theoretical curves in the figure are consistent, with minimal error, further confirming the accuracy of the dynamic model of the robot's propulsion force during swimming.

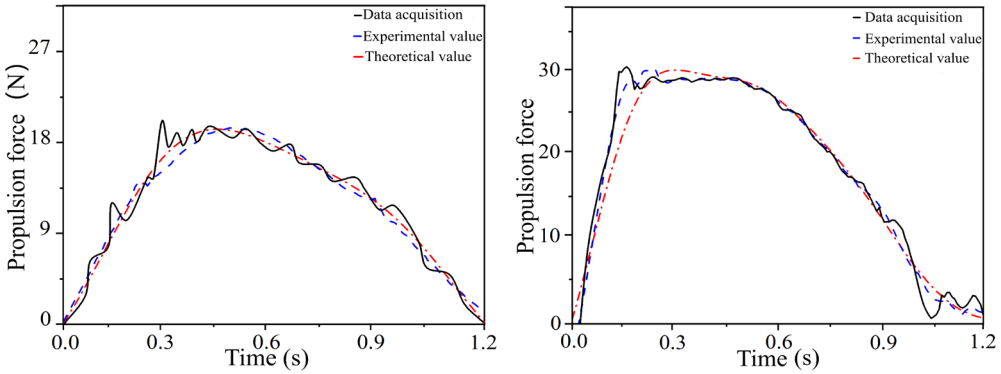

(a) Hip joint angular velocity is 0° (b) Hip joint angular velocity is 1.9rad/s

Figure 25. Propulsive force curve in propulsive phase.

4.3. Prototype Frog-Style Jumping Test

Based on equations (35) and (37) in Chapter 4.1, it can be concluded that the jump height and distance determine the robot's jumping performance. The key parameters affecting this are the takeoff posture angle θ_a and the explosive force output Fz from the detonator. Therefore, the preferred approach in the experiment (**See video 2**) is to drive the forelimb mechanism of the prototype,

 doi:10.20944/preprints202604.2226.v1

allowing the driving angle θ_0 to vary between 0° and 90°, which results in the change of the robot's takeoff posture angle θ_a from 0° to 80°, as shown in figure 26 (a~c). Meanwhile, the driving angle θ_0 from equations (32) is input with a specific value. After theoretical calculation, both the theoretical and experimental values are plotted together in figure 26(d). The error between the theoretical and experimental values in figure 26(d) is minimal, and the trends align closely. This verifies the correctness of the theoretical derivation of the takeoff posture angle and demonstrates the robot's ability to adjust the takeoff posture angle through its front limbs.

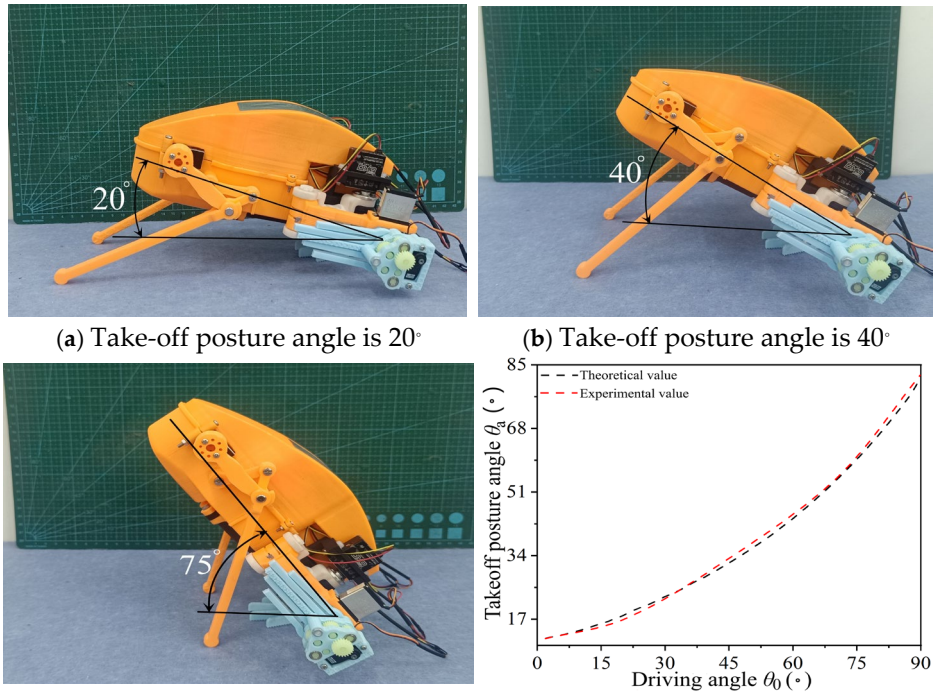

(**a**) Take-off posture angle is 20° (**b**) Take-off posture angle is 40°

(**c**) Take-off posture angle is 75° (**d**) Take-off posture angle output curve

Figure 26. Change in the robot's take-off posture angle adjustment.

Additionally, by programming the control of the forelimbs and the gas delivery system, the robot performs frog-like jumping experiments with varying amounts of hydrogen-oxygen mixed gas at different posture angles. In this experiment, the combustion chamber is a trapezoidal prism, and both the hydrogen-oxygen mixture ratio and the ratio of the chamber's top and bottom surface areas are set to 2:1.By using a camera to record the entire experiment (**See video 3)**, key frames were extracted from the video to generate a sequence diagram of the robot's frog-style jumping posture, as shown in figure 27.In the motion sequence diagram, the corresponding transitional positions are annotated: point A represents the initial position, point B indicates the peak position, and point C denotes the final position.

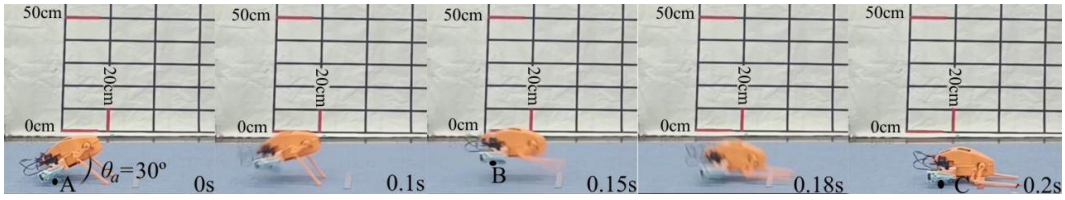

(**a**) Under the volume of 21ml, the take-off posture angle is 30°

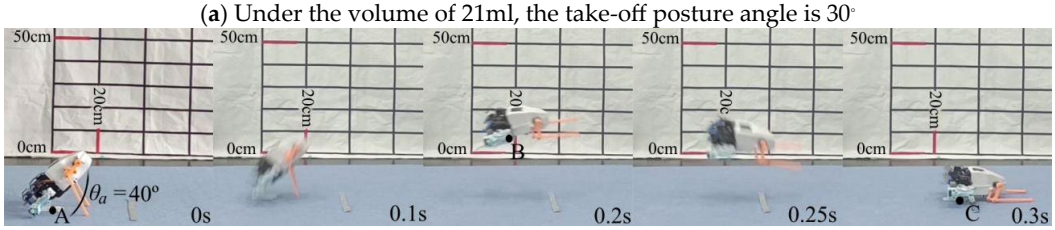

(b) Under the volume of 21ml, the take-off posture angle is 40°

 doi:10.20944/preprints202604.2226.v1

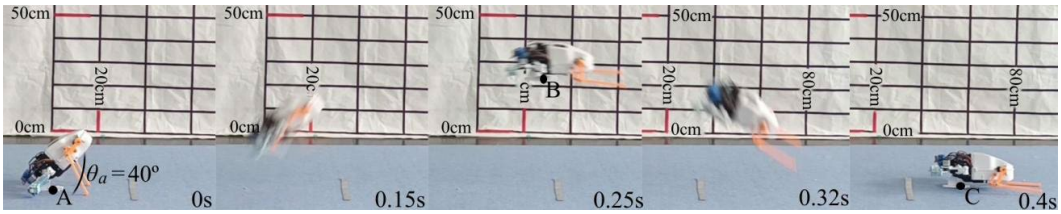

(c) Under the volume of 27ml, the take-off posture angle is 40°

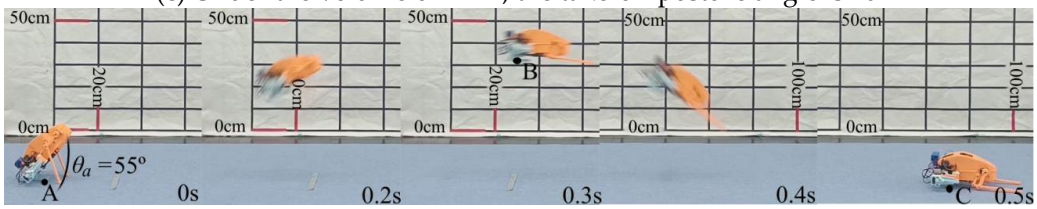

(d) Under the volume of 33ml, the take-off posture angle is 55°

Figure 27. Robot jumping experiment.

In figure 27(a), the robot's takeoff posture angle θ_a is 30 degrees. During a single jump, it achieved a height of 50 mm and a distance of 100 mm. However, in figure27(b), the robot adjusts the takeoff posture angle θ_a to 40 degrees. During a single jump, both the height and distance are significantly greater than those in figure 27(a), with a jump height of 100 mm and a jump distance of 230 mm. Similarly, compared to figure 27(b), With the takeoff posture angle θ_a unchanged in figure 27(c), the mixed gas volume is increased by 6 ml, resulting in a jump height of 230 mm and a jump distance of 460 mm. This outcome is significantly greater than the jump height and distance in figure 27(b). Compared to figure 27(c), the robot increases the takeoff posture angle by 15 degrees in figure 27(d), the mixed gas volume is increased by 6 ml, resulting in a jump height of 330 mm and a jump distance of 820 mm. This outcome is significantly greater than the jump height and distance in figure 27(c). Therefore, it can be concluded that by altering the takeoff posture angle and the mixed gas volume in the chamber, the robot can achieve different frog-like jump effects.

Based on the above experiments, multiple experimental studies were conducted with takeoff posture angle and the volume of mixed gas in the combustion chamber as input variables. Theoretical calculations were performed on equations (35) and (37). The experimental data and theoretical values were compiled and analyzed, resulting in characteristic curves that reflect the impact of these factors on the robot's jumping performance, as shown in figure 28(a~b). From figure 28(a), it can be observed that when the robot's takeoff posture angle is fixed, as the amount of mixed gas injected into the detonation chamber of the explosive driver increases, the robot's jumping height and distance will increase.

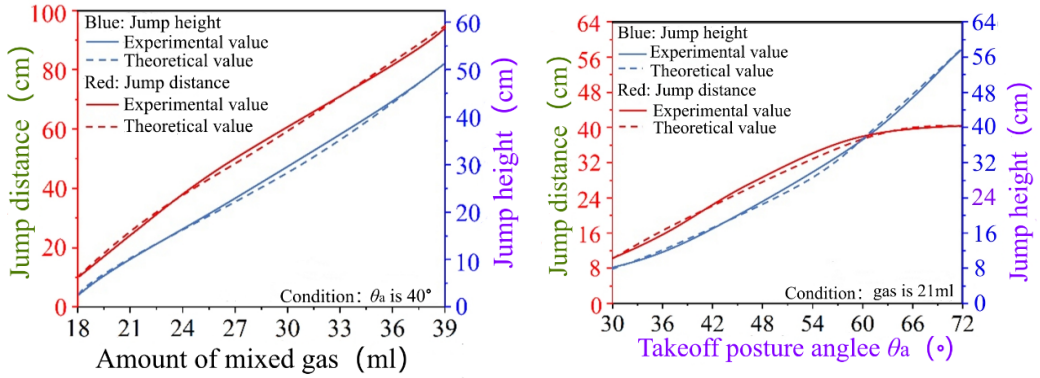

(**a**) Based on gas volume (**b**) Based on posture angle

Figure 28. Robot jumping motion performance curve.

From figure 28(b), it can be seen that when the amount of hydrogen-oxygen mixed gas injected is fixed, the robot's jumping height increases as the takeoff posture angle increases within the range

 doi:10.20944/preprints202604.2226.v1

of [30°, 72°]. The jumping distance increases as the takeoff posture angle increases within the range of [30°, 60°], but decreases as the angle increases within the range of [60°, 72°].This demonstrates that the robot's frog-like jump height and distance increase approximately proportionally with the amount of mixed gas injected. The injected gas volume determines how high and far the robot can jump. The robot's frog-like jump height increases approximately proportionally with the takeoff angle, while the jump distance first increases approximately proportionally with the takeoff angle and then decreases approximately inversely. The takeoff angle determines the optimization of the robot's efficiency in terms of height or distance during the jump. Additionally, the experimental data curves in figure 28 (a~b) closely match the theoretical values, with only a negligible error between them. Therefore, this validates the correctness of the theoretical derivation. In conclusion, the robot is capable of achieving high-performance frog-like jumping motion.

4.4. Prototype Amphibious Frog-like Test

To further verify the amphibious mobility of the robot in a water-land alternating environment, a comprehensive experiment involving swimming and jumping was conducted on the robot. The experimental process consisted of swimming from the pool edge to a shallow slope, jumping from the shallow slope to a land platform, jumping from the land platform into the water, and then continuing to swim back to the pool edge. The pool was set with a length of 5000mm, a width of 2000mm, and a height of 800mm. After recording with a camera, the experimental video results were processed into screenshots (**See video 4**), resulting in a sequence of amphibious motion images of the robot, as shown in figure 29 (a~d).As shown in figure 29 (a) and 30 (a), the robot completed three frog-like swimming strokes in the first segment within 17.5 seconds, successfully swimming from the pool edge to the shallow slope. The swimming distance was 1200mm, with an average speed of 68mm/s. Subsequently, the robot completed its first frog-like jump within 1 second, successfully leaping onto the land platform. The jump height and distance were 360mm and 1000mm, respectively, as shown in figure 29 (b) and 30 (b).

(a) Swim from edge of pool to shallow slope

(d) Jump from shallow slope to landing platform

(c) Jump into water on platform

 doi:10.20944/preprints202604.2226.v1

(d) Swim in the water to edge of pool

Figure 29. Robot amphibious movement experiment.

Then, the robot completed its second frog-like jump within 1 second, leaping from the land platform into the water. The jump height and distance were 300mm and 1200mm, respectively, as shown in Figures 29 (c) and 30 (b). Finally, the robot completed three frog-like swimming strokes in the second segment within 12.6 seconds, successfully swimming from the water back to the pool edge. The swimming distance was 1000mm, with an average speed of 79mm/s, as shown in figure 29 (d) and 30 (a). This validates the robot's amphibious mobility, capable of both swimming in water and jumping on land.

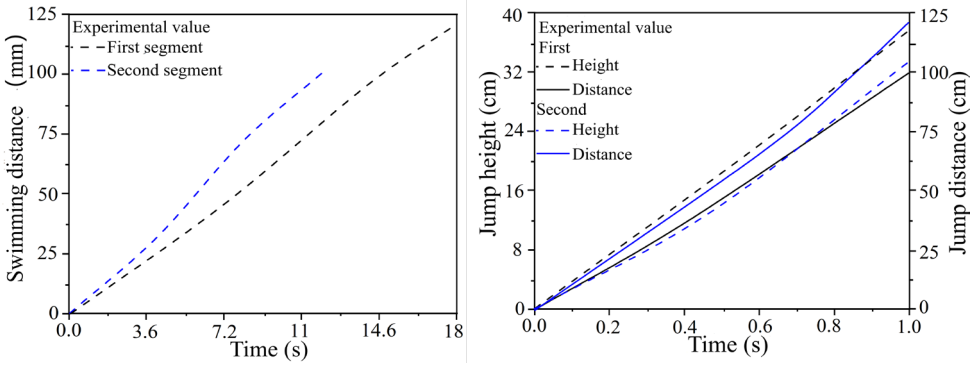

(**a**) Swimming movement (**b**) Jumping movement

Figure 30. Changes in robot amphibious motion.

Based on the previous experimental studies, Table 1.3 presents the specific parameter values achieved by the robot during the experiment. Compared to existing frog-like jumping robots or swimming robots, the data in the table show that this robot demonstrates continuity in both jumping and swimming, exhibiting amphibious mobility. Its swimming speed, jump height, and jump distance are all at an intermediate level, while it also features a lightweight design, showing good adaptability to both aquatic and terrestrial environments. Thus, the feasibility and correctness of the structural design, theoretical modeling, motion planning, and control system of this type of frog-like hybrid-driven amphibious robot have been verified, laying the foundation for future research on the motion of bio-inspired amphibious robots.

Table 1.3. Verifying robot design specifications.

Name	Weight	Swimming speed	Jumping Height	Jumping Distance
Parameter	600g	79mm/s	650mm	1200mm

5. Conclusions

Inspired by the amphibious motion characteristics of the biological frog, this paper presents the design of a novel frog-like hybrid drive amphibious robot for both land and water. The robot is based on an explosive-driven jumping mechanism and a rope-linked swimming system, enabling amphibious frog-like motion on land, in water, and across media. It also avoids the need for complex structural switching during transitions between land and water environments. Based on this, a frog-like hybrid power model was established, and the high-energy instantaneous explosive force

 doi:10.20944/preprints202604.2226.v1

generated during the frog-like jumping motion, as well as the high-density hydrodynamic force during swimming, were calculated. Subsequently, by combining the amphibious motion characteristics of frogs with the structural features of the robot, the high-performance frog-like jumping ability achieved through explosive drive on land and the efficient frog-like swimming ability achieved through rope drive in water were analyzed. Finally, a prototype of the robot was built to validate its frog-like amphibious motion on both land and water. This not only confirmed the feasibility of the robot's amphibious mechanism but also proved the correctness and effectiveness of the amphibious power theory modeling and its motion capabilities.

Supplementary Materials: The following supporting information can be downloaded at the website of this paper posted on Preprints.org, https://pan.baidu.com/s/1v9M1tcTtR706o6XiNHXS6g?pwd=a8eg extraction code: a8eg. 1. Experiment video 1, related to Figure 24. 2. Experiment video 2, related to Figure 26. 3. Experiment video 3, related to Figure 27. 4. Experiment video 4, related to Figure 29.

Author Contributions: Conceptualization, methodology, Formal analysis and Writing—original draft,Y. T. -P.; software, L. B. -H. ; validation,investigation, resources,funding acquisition,and writing—review and editing, Y.S.-O; visualization, project administration, J.Z.-F; All authors have read and agreed to the published version of the manuscript.

Funding: This research was financially supported by Natural Science Foundation of China (Grants No. 62173319) , Liaoning Province International Science and Technology Cooperation Program (2024JH2/101900001),and Shenzhen Technology Project (JCYJ20220818101211025) .

Institutional Review Board Statement: In this section, please add the Institutional Review Board Statement and approval number for studies involving humans or animals. You might choose to exclude this statement if the study did not require ethical approval. Please note that the Editorial Office might ask you for further information. Please add “The study was conducted in accordance with the Declaration of Helsinki, and approved by the Institutional Review Board (or Ethics Committee) of NAME OF INSTITUTE (protocol code XXX and date of approval).” for studies involving humans. OR “The animal study protocol was approved by the Institutional Review Board (or Ethics Committee) of NAME OF INSTITUTE (protocol code XXX and date of approval).” for studies involving animals. OR “Ethical review and approval were waived for this study due to REASON (please provide a detailed justification).” OR “Not applicable” for studies not involving humans or animals.

Informed Consent Statement: The informed consent form was signed by all the participants included in the tests.

Data Availability Statement: Data are contained within the article.

Conflicts of Interest: The authors declare no conflicts of interest.

References

1. Su, X.;Pan, Q.;Wang, H.;Ren, Z.. Research Progresses of Robots with Active Deformable Materials.Robot .2021, 43(1),112-128.
2. Wang, X.;Jia, S.;et al. Optical-driven miniature robots: driving mechanism, applications and future trends. Lab on a Chip .2025,25(18),4473-4507.
3. Jongkuk, K.; et al.High-performance Electrified Hydrogel Actuators Basedon Wrinkled Nanomembrane Electrodes for Untethered Insect-scale Soft Aquabots. Sci. Robot. 2022,7,eabo6463.
4. Jiseong, S.; Babar, J.;et al. Thermo-pneumatic Artificial Muscle: Air-based Thermo-pneumatic Artificial Muscles for Pumpless Pneumatic Actuation. Soft Robotics.2024,11(2),187-197.
5. Nwafor, C. J.;Girerd, C. ;et al. Design and Fabrication of Concentric Tube Robots: a Survey. In IEEE Transactions on Robotics.2023,39(4),2510-2528.
6. Wang, Y.;Deng, J.;Te, T.; et al.Review of Research on 3D Printing Manufacturing Technology of Soft Robots. Journal of Mechanical Engineering.2021,57(15),186-198.

 doi:10.20944/preprints202604.2226.v1

7. Yin, K.; Gao, Y.; Gao, F.; et al. Mechanism Design and Motion Planning of a Hexapod Curling Robot Exhibited During the Beijing 2022 Winter Olympics Games.Engineering .2022,35,15-31.
8. Ceylan, H.;Giltinan, J.;Kozielski, K.; et al.Mobile Microrobots for Bioengineering Applications. Lab on a Chip .2017,17(10),1705-1724.
9. Zhou, X.; Zhong, H.; Zhang, H.;et al. Current Status, Challenges, and Prospects for New Types of Aerial Robots.Engineering .2024,41,19-34.
10. Qian, X.;Zhan, J.;Ma, J.;Dou, J.Literature Review on Design of Mobile robots.Packaging Engineering.2025,46(12),13-39+601.
11. Dinh, N.; Vosbein, D.; Wang, Y., Cui Q. Reinforcement Learning-Enabled Control and Design of Rigid-Link Robotic Fish: A Comprehensive Review. Sensors. 2026,26(3):996.
12. Yu, F.;Chen, Y.Trajectory Tracking Control of an Amphibian Robot with Operational Capability.International Journal of Advanced Robotic Systems.2019,16(4),1.
13. Hou, X.; Guo, S.; Shi, L.; Xing, H.;Liu, Y.; Liu, H;.Hu, Y.;Xia, D.;Li, Z. Hydrodynamic Analysis-Based Modeling and Experimental Verification of a New Water-Jet Thruster for an Amphibious Spherical Robot. Sensors. 2019,19(2):259.
14. Zhong, G.;Gao, J.;Chai, X.;et al.Design and Performance Analysis of a Triphibious Robot with Tilting-rotor Structure.IEEE Access. 2021,9,10871-10879.
15. Kong, J.;Niu, S.;Lu, P.; et al.Design of a Bio-inspired Water-ground-air Amphibious and Cross Domain Robot Platform.In: 2022 IEEE International Conference on Robotics and Biomimetics (ROBIO) in Jinghong , 2022;pp. 2177-2182.
16. Chen,Y.;Zhang,S.;Zhang, L.;et al.A Dual-mode Underwater robot with Non-contact Adsorption Ability: Design, Mode Switching and Field Applications.Ocean Engineering.2025,330,1-11.
17. Evangeliou, N.;Chaikalis, D.;Giakoumidis, N.;et al.Mechatronic Design of an Amphibious Drone .In: 2023 9th International Conference on Automation, Robotics and Applications(ICARA) in Abu Dhabi,2023; pp. 230-233.
18. Wang, R.;Wang, S.;Wang, Y.;et al.Development and Motion Control of Biomimetic Underwater Robots: a Survey. IEEE Trans Syst Man Cybern Syst.2022,52(2),833-844.
19. Bai, X.; Shang, J.; Luo, Z.;et al.Development of Amphibious Biomimetic Robots.Journal of Zhejiang University-SCIENCE A . 2022,23(3),157-187.
20. Wang, P.; Liu, X.; Song, A.; et al.Actuation and Locomotion of Miniature Underwater Robots: A Survey.Engineering.2025,51,195-21.
21. Zhang, J.; Zhou, J.;Yuan, S.; et al.Review of Configuration,Motion Mechanism, Modeling and Control of Amphibious Bionic Robots. Robot . 2023,45(3),367-384.
22. Qian, Q.;Wang, K.;Song, Z.; et al.Optimal Design of Self-adaptive Climbing Mechanism for Landing in the Amphibious Bionic Robot. Journal of National University of Defense Technology .2023,45(1),208-214.
23. Xu, X.;Liu, B.;Pan, D.;et al.Research and Application of Amphibious Bionic Robots.Journal of Unmanned Undersea Systems . 2023,31(1),143-151.
24. Ma, J.; Hu, J.;Zhu, G.;et al.Research Status and Progress of Military Bionic Robot Based on Design Morphology. Packaging Engineering.2022,43(4),1-11.
25. Ren, K.;Yu, J. Research Status of Bionic Amphibious Robots: a Review. Ocean Eng . 2021,227,108862.
26. Ma, X.;Wang, G.;Liu, K.;et al. Design and Optimization of a Multimode Amphibious Robot with Propeller-leg. IEEE Trans Robot.2022,38(6),3807-3820.
27. Lu, L.;Gao, X.;Xiang, M.;Yan, Z.;Han, B.Design of a Variable Wheel-propeller Integrated Mechanism for Amphibious Robots. In:2024 IEEE/RSJ International Conference on Intelligent Robots and Systems (IROS) in Abu Dhabi,2024;pp.3519-3525.
28. Sato, T.; Oda, T.; Sato, T.; Yamashita, Y.; et al. Amphibious Robot with Horizontal Articulated Mechanism.In:2025 1st International Conference on Consumer Technology (ICCT-Pacific) in Shimane,2025; pp. 1-4.
29. Xu, P.;Wang, Z.; Lin, H.;et al. Research on Screw Propulsion Performance of Amphibious Robot. Journal of Unmanned Undersea Systems .2024,32(6),1063-1071.

 doi:10.20944/preprints202604.2226.v1

30. Hu, S.;Li, L.Network Entropy, Disequilibrium and Complexity in Computing and Networks Convergence.Journal of Jiamusi University(NaturalScienceEdition) .2025,43(2),17-19+26.
31. Ohashi, H.; Shigaki, S.; et al.Development of Bio-cultured Artificial Muscles with High Design Flexibility.J Bionic Eng.2023,20,1635-1645.
32. Zhou, S.;Zhang, W.; Zou,Y.; et al.Piezoelectric Driven Insect-inspired Robot with Flapping Wings Capable of Skating on the Water. Electronics Letters.2017,53(9),579-580.
33. Qin, M. Design and Research of Dragonfly Robot Under the Background of Artificial Intelligence.Wireless Communications and Mobile Computing.2022,1-7.
34. Zhao, W.;Zhang, Y.;Yang, L.; et al.Research and Implementation of Pneumatic Amphibious Soft Bionic Robot. Machines.2024,12(6),12:393.
35. Baines, R.; Patiballa, S.;Booth, J.; et al.Multi-environment Robotic Transitions Through Adaptive Morphogenesis.Nature.2022,610(7931),283-289.
36. Hwang, J.; Wang, W.;Shape Memory Alloy-based Soft Amphibious Robot Capable of Seal-inspired Locomotion. Advanced Materials Technologies.2022,7(6),2101153.
37. Xia, M.; Wang, H. ;Yin, Q.; et al. Design and Mechanics of a Composite Wave-driven Soft Robotic Fin for Biomimetic Amphibious Robot.J Bionic Eng. 2023,20(3),934-952.
38. Wang, X.;Wu, Q.;Wang, Y.; et al. Structure Design, Kinematic Modeling, and Motion Planning of Novel Ray-inspired Amphibious Robots. Chinese Journal of Engineering.2024,46(9),1594-1603.
39. Cocuzza, S.;Doria, A.;Reis, M.Vibration-based Locomotion of an Amphibious Robot. Appl Sci. 2021,11(5),2212.
40. Guo, J. ; Li, C.; et al.Study on the Autonomous Multirobot Collaborative Control System Based on Spherical Amphibious Robots. IEEE Syst J .2020,15(4),4950-4957.
41. Niiyama, R.;Nagakubo, A.;Kuniyoshi, Y. Mowgli: Abipedal Jumping and Landing Robot with an Artificial Musculoskeletal System.In: IEEE International Conference on Robotics & Automation in Rome,2007;pp.2546-2551.
42. Ahn, J. ;Park, J.; Kim, J.;et al. Frog-inspired Jumping Robot for Overcoming High Obstacles.In:2013 IEEE ISR in Seou,2013;pp.1-4.
43. Gao, F.Design and Experiment of a Frog-inspired Soft Jumping Robot Driven by Combustion. Harbin: Harbin Institute of Technology .2012,19-41.
44. Fan, J.; Du, Q.;Dong, Z.; et al. Design of the Jump Mechanism for a Biomimetic Robotic Frog. Biomimetics.2022,7(4),142.
45. Qiu, Y.Research on Swimming Mechanism of the Frog and Mechanical Design of the Bionic Robot. Harbin: Harbin Institute of Technology .2007,29-39.
46. Fan, J.; Kong, P.;Yuan, B.; et al.Optimization of a Frog Inspired Robot Powered by Pneumatic Muscles .In: 2017 IEEE International Conference on Mechatronics and Automation (ICMA) in Takamatsu ,2017;pp. 602-607.
47. Fan, J.; Zhang, W.; Kong, P.;et al. Design and Dynamic Model of a Frog-inspired Swimming Robot Powered by Pneumatic Muscles.Chinese Journal of Mechanical Engineering.2017,30(5),1123-1132.
48. Tang, Y.; Qin, L.; et al. A Frog-inspired Swimming Robot Based on Dielectric Elastomer Actuators.In: 2017 IEEE/RSJ International Conference on Intelligent Robots and Systems in Vancouve, 2017;pp.2403-2408.
49. Gul, J.;Kin, K.; Lim, J.; et al.Fsi Modeling of Frog Inspired Soft Robot Embedded with Ald Encapsulated Flex Sensor for Underwater Synchronous Swim.In:2017 IEEE International Symposium on Robotics and Intelligent Sensors in Ottawa,2017;pp. 255–259.